

---

---

## ANALYSIS OF HELIO- AND GEOPHYSICAL EVENTS IN OCTOBER–NOVEMBER 2021 FROM COMPREHENSIVE OBSERVATIONS OF SHICRA SB RAS

---

---

**V.I. Kozlov** 

*Yu.G. Shafer Institute of Cosmophysical Research  
and Aeronomy SB RAS,  
Yakutsk, Russia, v.kozlov@ikfia.ysn.ru*

**S.A. Starodubtsev** 

*Yu.G. Shafer Institute of Cosmophysical Research  
and Aeronomy SB RAS,  
Yakutsk, Russia, starodub@ikfia.ysn.ru*

**V.G. Grigoryev** 

*Yu.G. Shafer Institute of Cosmophysical Research  
and Aeronomy SB RAS,  
Yakutsk, Russia, grig@ikfia.ysn.ru*

**D.G. Baishev** 

*Yu.G. Shafer Institute of Cosmophysical Research  
and Aeronomy SB RAS,  
Yakutsk, Russia, baishev@ikfia.ysn.ru*

**G.A. Makarov** 

*Yu.G. Shafer Institute of Cosmophysical Research  
and Aeronomy SB RAS,  
Yakutsk, Russia, gmakarov@ikfia.ysn.ru*

**E.A. Pavlov** 

*Yu.G. Shafer Institute of Cosmophysical Research  
and Aeronomy SB RAS,  
Yakutsk, Russia, pochta\_baki@mail.ru*

**R.R. Karimov** 

*Yu.G. Shafer Institute of Cosmophysical Research  
and Aeronomy SB RAS,  
Yakutsk, Russia, karimov@ikfia.ysn.ru*

**A.A. Korsakov** 

*Yu.G. Shafer Institute of Cosmophysical Research  
and Aeronomy SB RAS,  
Yakutsk, Russia, korsakovaa@ikfia.ysn.ru*

**A.E. Stepanov** 

*Yu.G. Shafer Institute of Cosmophysical Research  
and Aeronomy SB RAS,  
Yakutsk, Russia, a\_e\_stepanov@ikfia.ysn.ru*

**I.I. Koltovskoi** 

*Yu.G. Shafer Institute of Cosmophysical Research  
and Aeronomy SB RAS,  
Yakutsk, Russia, koltik@ikfia.ysn.ru*

**P.P. Ammosov** 

*Yu.G. Shafer Institute of Cosmophysical Research  
and Aeronomy SB RAS,  
Yakutsk, Russia, ammosov@ikfia.ysn.ru*

**G.A. Gavril'yeva** 

*Yu.G. Shafer Institute of Cosmophysical Research  
and Aeronomy SB RAS,  
Yakutsk, Russia, gagavril'yeva@ikfia.ysn.ru*

**I.B. Ievenko** 

*Yu.G. Shafer Institute of Cosmophysical Research  
and Aeronomy SB RAS,  
Yakutsk, Russia, ievenko@ikfia.ysn.ru*

**S.G. Parnikov** 

*Yu.G. Shafer Institute of Cosmophysical Research  
and Aeronomy SB RAS,  
Yakutsk, Russia, parnikov@ikfia.ysn.ru*

---

**Abstract.** The paper reports the results of comprehensive observations of space weather manifestations during geophysical events at the end of October – beginning of November 2021 at the Yakut meridional geophysical network of SHICRA SB RAS equipped with a complex of various scientific instruments installed at the stations Yakutsk, Maimaga, Zhigansk, and Tixie Bay (neutron monitors, an ionosonde, a riometer, receivers of VLF radio noise and signals from navigation radio stations, magnetometers), as well as a complex of optical instruments installed in Maimaga. We present the results of the analysis of phenomena occurring in near-Earth space, Earth's ionosphere and atmosphere in the North-Eastern sector of Siberia. We examine the properties of the geophysical effects of space weather observed at this time: Forbush decreases of cosmic rays, geomagnetic storm and substorm, riometric absorption,

the occurrence of electrojet, quasi-periodic broadband radio hisses, assess changes in the effective height of the Earth–ionosphere waveguide, F2-layer critical frequencies, absorption of short-wave radio waves, temperature of the neutral atmosphere, radiant auroral band in 557.7 and 630.0 nm emissions, as well as the region of intense auroras and auroral red arc (SAR arc).

**Keywords:** solar flare, magnetic storm, Forbush decrease, aurora, auroral arc, neutron monitor, ionosonde, riometer, receiver of VLF radio noise and signals from navigation radio stations, magnetometers.

---

## INTRODUCTION

Solar activity (SA) cycle 25 began in December 2019 and therefore the sharp increase in geophysical ac-

tivity in late October and early November 2021 during the initial growth phase of the next 11-year solar cycle is quite unexpected.

Only from October 26 to November 2, 2021, seven class M and one class X flares were recorded on the Sun, which occurred in one active region (AR) AR12887. Along with them, coronal mass ejections (CMEs) were repeatedly observed [[https://cdaw.gsfc.nasa.gov/CME\\_list](https://cdaw.gsfc.nasa.gov/CME_list)]. As a result, significant changes in space weather occurred in near-Earth space, and hence an increase in solar cosmic ray (SCR) fluxes was detected on Earth, and the second strong magnetic storm with minimum  $Dst < -105$  nT was recorded in the current solar cycle.

### CR INTENSITY VARIATIONS AS OBSERVED AT THE TIXIE BAY AND YAKUTSK STATIONS

The most powerful solar flare (X1.0) during this period with a maximum X-ray emission on October 28, 2021 at 15:35 UT occurred in AR12887 and had coordinates S28W02. At the same time, strong ultraviolet radiation and type II and IV radio emissions were recorded [<https://www.spaceweather.com>, <https://solarmonitor.org>]. This flare caused the first increase in SCR flux recorded on Earth in SC 25. This event was the 73rd since the first SCR flare observed on February 28, 1942.

It is now known as GLE73 (Ground Level Enhancement). The increase was small, and its amplitude was  $<6\%$  even at polar CR stations. Figure 1 presents pressure-corrected 1-min data on this event from neutron monitors (NM) 18-NM-64 at the Tixie Bay station and 24-NM-64 at the Yakutsk station. At that time, both stations were on the nightside of Earth, and the increase in CR intensity in the data from these stations was very weak, almost invisible for current measurements (see Figure 1). As a GLE event it can be reliably identified only by using additional information from the well-known Real-Time Database for High-Resolution Neutron Monitor Measurements (NMDB, [<http://www.nmdb.eu>]).

The M1.7 class solar flare (S27W76) that occurred a few days later, on November 2, 2021, in the same AR [<https://solarmonitor.org>], caused the first powerful Forbush effect (FE) in SC 25, which began at the end of November 3. Its amplitude, according to the pressure-

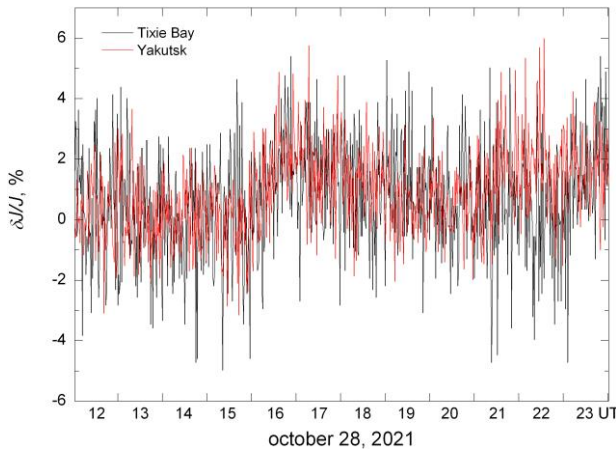


Figure 1. Ground level enhancement in CR intensity during the GLE73 event according to data from the Tixie Bay and Yakutsk neutron monitors

corrected 1-min NM data from the Tixie Bay station, was as high as 18.9 %; and from the Yakutsk station, 16.1 % (Figure 2). The complex structure of the decrease in CR intensity is due to the structure of interplanetary CME (ICME) arriving at Earth's orbit, which had a speed of  $\sim 1470$  km/s [[https://cdaw.gsfc.nasa.gov/CME\\_list](https://cdaw.gsfc.nasa.gov/CME_list)].

Note that the ICME structure is generally thought to consist of three parts: an interplanetary shock (IS), a region of turbulence behind it, and a following magnetic cloud (MC) [Howard, 2011]. In this case, IS is the first part of CME and is generated when the CME itself propagates at a super-Alfvénic velocity relative to the solar wind (SW). The second part (the turbulence region) results from the interaction of IS with background SW parameters and features a high level of their fluctuations. The third part in CME development is MC. It is a plasma cloud moving from a source on the Sun, which, in particular, exhibits a strong regular slowly rotating magnetic field with low concentration and temperature of SW plasma.

Since 2009, SHICRA SB RAS has been monitoring the CR intensity in real time to predict ground-level effects of space weather. For this purpose, along with others we adopt the harmonic analysis method that also uses pressure-corrected 1-hour data from NMs installed at the Tixie Bay and Yakutsk CR stations [Grigoryev et al., 2008; Krymsky et al., 2003]. As an example, Figure 3, *a, b* presents the results of identification of parameters of the first harmonic of CR anisotropy simultaneously at the Tixie Bay and Yakutsk stations. At the top are names of the stations, the type of detectors, and projection onto the XY plane of the GSE coordinate system in use that shows the length of the unit vector of the first harmonic (diurnal) of CR anisotropy. At the bottom is the time dependence of the CR anisotropy vector per se; and below, its corresponding CR intensity. Note that the Tixie Bay and Yakutsk CR stations are spaced over a distance  $>1200$  km and have their own power sources, thus the measurements made at them are completely independent. Projections of the CR anisotropy vectors are highlighted in red if they simultaneously exceed 0.3 % at both stations and are antisunward, which increases

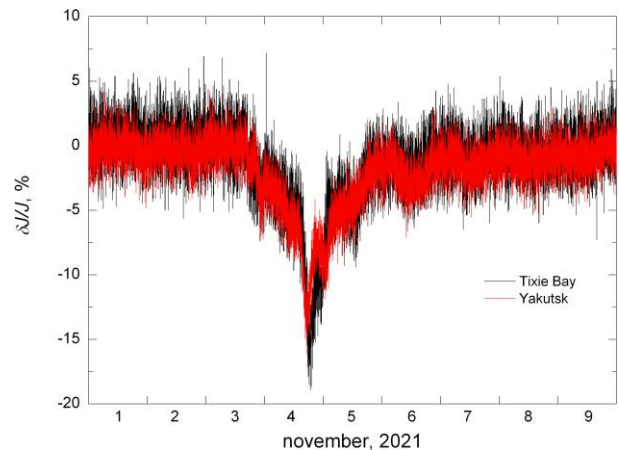


Figure 2. Forbush effect as measured by Tixie Bay and Yakutsk neutron monitors

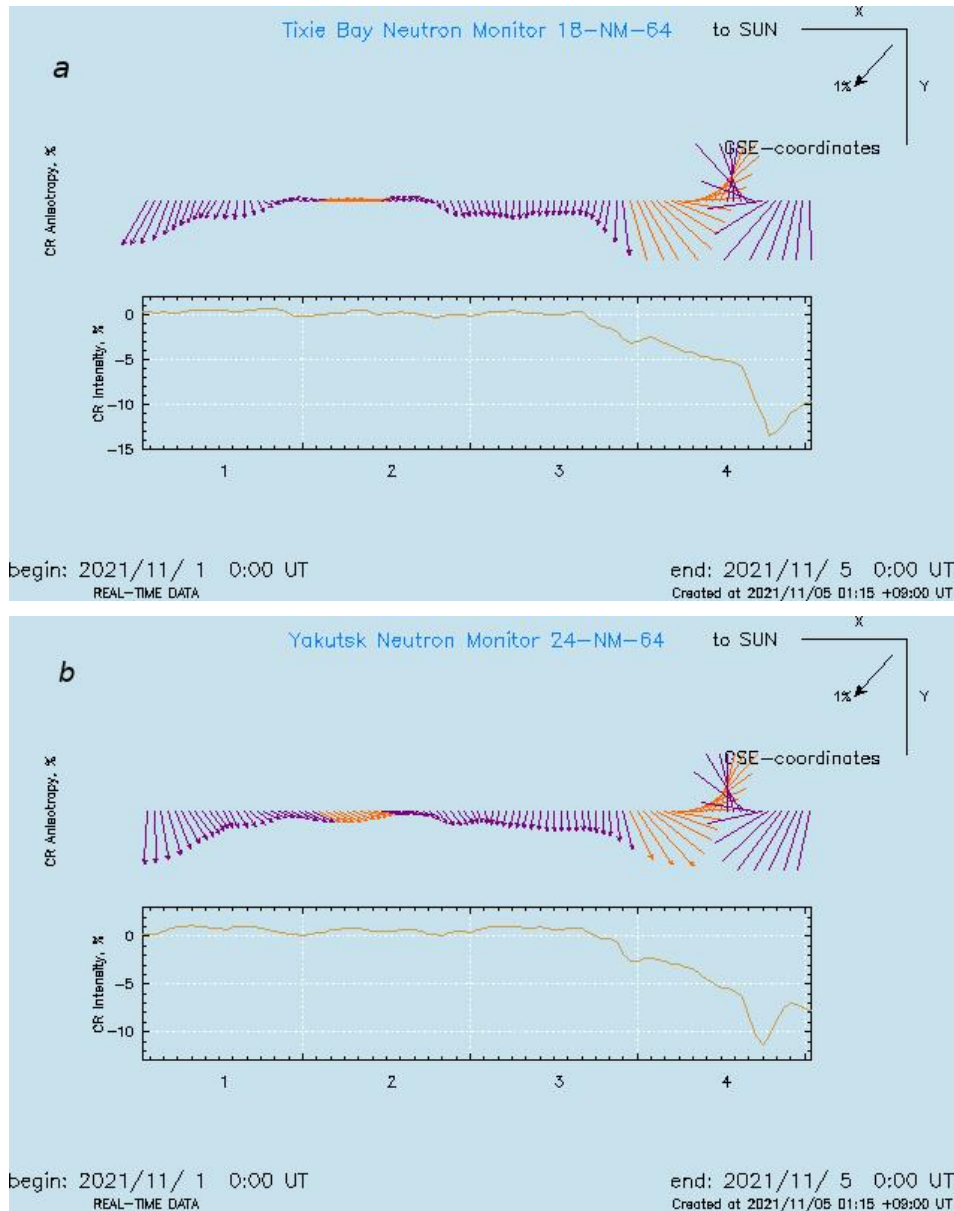


Figure 3. Results of prediction of a large-scale SW disturbance approaching Earth as measured by the Tixie Bay and Yakutsk neutron monitors

Figure 3, *a, b* indicates that the above changes in CR anisotropy parameters started at the beginning of November 2, and FE itself began more than a day later, on November 3, 2021, at  $\sim 16:00$  UT. Note that during the very decrease in CR intensity Earth was in disturbed SW behind the IS front, so the anisotropy parameters are significantly distorted and should not be taken into account when analyzing the event.

### GEOMAGNETIC VARIATIONS IN NOVEMBER 2021, THEIR CONNECTION TO THE INTERPLANETARY CONDITIONS

Figure 4 illustrates the dynamics of the geomagnetic index  $Dst$  in November 2021 [[https://wdc.kugi.kyoto-u.ac.jp/dst\\_provisional/index.html](https://wdc.kugi.kyoto-u.ac.jp/dst_provisional/index.html)]. It can be seen there were large geomagnetic disturbances. According to the

classification [Loewe, Prolls, 1997], they can be classified as strong magnetic storms. During the magnetic storm main phase, hourly average  $Dst$ , according to preliminary data, ran to  $-105$  nT. Since September 2017, only three storms of the same level have been recorded on Earth: May 12, 2021, May 14, 2019, August 26, 2018.

Figure 5 illustrates changes in the mid-latitude geomagnetic indices  $ASY-H$  and  $SYM-H$  ( $SYM-H$  is similar to  $Dst$ , but has 1-min time resolution), as well as in the SW velocity  $V$  and IMF  $B$  modulus [<https://spdf.gsfc.nasa.gov/pub/data/omni/>]. The magnetic storm, as shown in Figure 5 according to geomagnetic index data, had a sudden commencement on November 3 at 19:48 UT. We can assume that this storm results from the interaction of Earth's magnetosphere with the CME-type high-velocity SW structure characterized by strong IMF. Note that the geomagnetic indices did not respond strongly to the previous structure with increases in  $V$  and  $B$

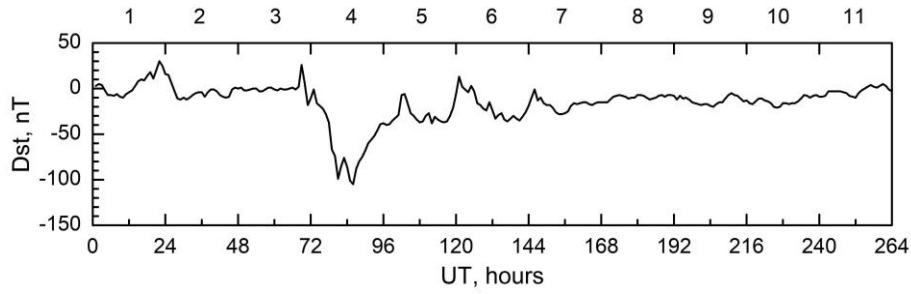


Figure 4. *Dst* variations in early November 2021. Begin time is November 1 in hours; the days of the period in question are at the top

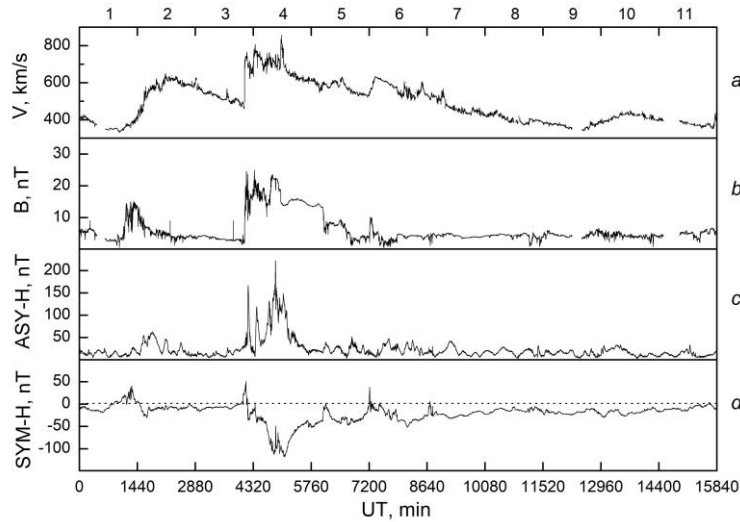


Figure 5. SW velocity  $V$  (a), IMF  $B$  (b), and mid-latitude geomagnetic indices  $ASY-H$  (c) and  $SYM-H$  (d) on November 1–11, 2021. The dotted horizontal line is the zero value of  $SYM-H$ . Begin time here and in the following figures is November 1 in minutes; the days of the period in question are shown at the top

on November 1, changing by no more than 40 nT ( $SYM-H$ ) and 60 nT ( $ASY-H$ ).

In the initial and main phases of the November 3–5, 2021 storm, the stations Yakutsk (corrected geomagnetic coordinates: latitude  $\Phi' \approx 56^\circ$  N, longitude  $\Lambda' \approx 201^\circ$  E), Zhigansk ( $\Phi' \approx 61^\circ$  N,  $\Lambda' \approx 194^\circ$  E), and Kotelny Island ( $\Phi' \approx 70^\circ$  N,  $\Lambda' \approx 201^\circ$  E) recorded strong geomagnetic disturbances. At the Yakutsk and Zhigansk stations, fluxgate magnetometers MAGDAS-9 were employed to detect geomagnetic variations [Baishev et al., 2017], and on Kotelny Island, a fluxgate magnetometer DCR-3 [Yumoto et al., 1992]. Figure 6 shows changes in the magnetic field horizontal  $H$  and vertical  $Z$  components at these stations, as well as in mid-latitude  $ASY-H$  (c) and  $SYM-H$  (d) during these days.

It can be seen that on Kotelny Island on November 3 at 20:10 UT there was a sharp decrease in the magnetic field  $H$  component by  $\sim 900$  nT relative to the quiet level; at the Zhigansk station, the same decrease began at 21:00 UT. The field at these stations returned back to the quiet level at  $\sim 23:10$  UT. The Yakutsk station at that time observed oscillatory changes in the  $H$  component with an amplitude to 90–120 nT and a period  $\sim 16$ –20 min. The oscillatory changes in  $H$  were also seen at the Zhigansk station, but they had relatively lower amplitude against the background of a large negative bay. As for the  $Z$  component, at the

Zhigansk station it decreased by  $\sim 840$  nT (with significant oscillations); and at the Yakutsk station, by 180 nT (with low-amplitude oscillations). Negative magnetic field  $H$ ,  $Z$ , and  $D$  components indicate that a westward electrojet developed in the ionosphere north of the Zhigansk station, which deflected by  $\sim 34^\circ$  north of the latitude. We can assume that this magnetic field disturbance is an isolated intense substorm.

According to the data on auroral indices during this period,  $AU > 500$  nT and  $AL < -1500$  nT [[https://wdc.kugi.kyoto-u.ac.jp/ae\\_realtime/](https://wdc.kugi.kyoto-u.ac.jp/ae_realtime/)]. According to the data from the global magnetometer network SuperMag [<https://supermag.jhuapl.edu/>], the distribution of magnetic vectors obtained from observational data and model calculations corresponds to current systems DP11 and DP12 [Yakhnin, 2008]. In the sunlit hemisphere, the  $SML$  and  $SMU$  indices measuring intensities of westward and eastward electrojets [<https://supermag.jhuapl.edu/>] are comparable and run to  $-900$  and  $730$  nT respectively, whereas in the nightside hemisphere the  $SML$  index of the westward electrojet ( $-1500$  nT) significantly exceeds  $SMU$  of the eastward electrojet (520 nT). The pattern of changes in the magnetic field  $H$  component on Kotelny Island, at the Zhigansk and Yakutsk stations, located in the dawn sector during the development of the substorm, fits perfectly into the distribution of the calculated magnetic vectors from

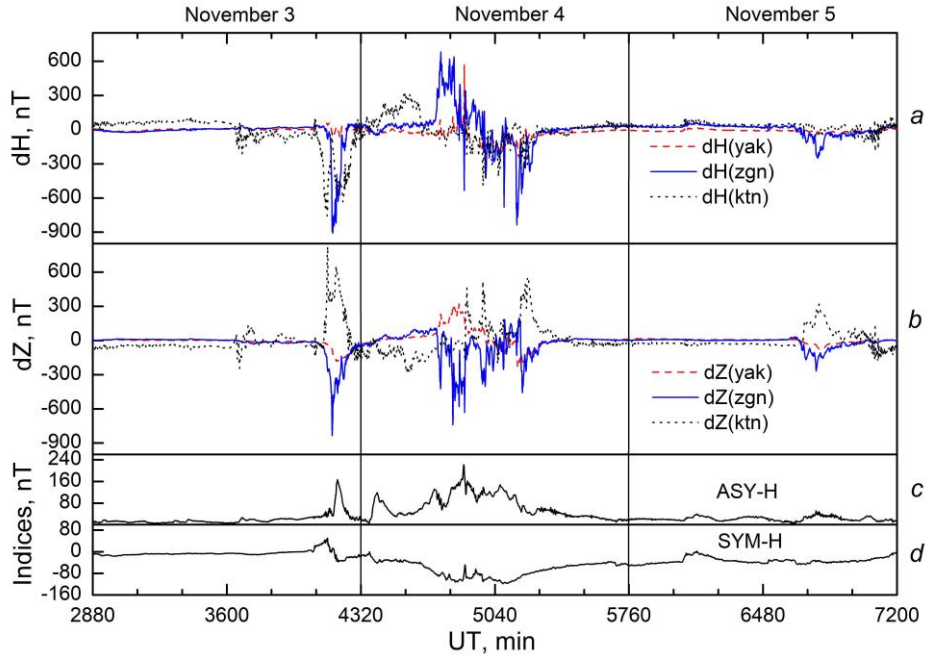


Figure 6. Horizontal  $dH$  (a) and vertical  $dZ$  (b) components of the magnetic field at the stations Yakutsk (yak), Zhigansk (zgn), and Kotelny Island (ktn), as well as mid-latitude  $ASY-H$  (c) and  $SYM-H$  (d) on November 3–5, 2021. Solid vertical lines in this and following figures correspond to 00:00 UT

SuperMag as part of DP11. Figure 7, *a* exhibits the distribution of horizontal magnetic vectors calculated from AMPERE project data [<https://ampere.jhuapl.edu/>] to illustrate the direction of the ionospheric equivalent current in the period 21:04–21:14 UT. In the dawn sector at latitudes  $65^\circ < \Phi' < 69^\circ$ , an auroral westward electrojet can be identified. Figure 7, *b* illustrates the distribution of field-aligned currents as derived from AMPERE data [<https://ampere.jhuapl.edu/>]. In the dawn sector, field-aligned currents are seen to flow into the ionosphere at  $\sim 68^\circ$ – $72^\circ$  N and flow out at  $\sim 64^\circ$ – $66^\circ$  N. From this we can conclude that the «center of gravity» of the westward electrojet is at  $\sim 67^\circ$  N.

The data on mid-latitude  $ASY-H$  and  $SYM-H$  presented in Figure 5, *c*, *d* suggests that at  $\sim 19:48$  UT there was a noticeable jump in  $SYM-H$  by 20 nT to the region of positive values, which persisted until 21:17 UT, running to 50 nT at 20:57–21:00 UT. Afterwards, at  $\sim 21:34$  UT, a sharp increase in  $ASY-H$  and a decrease in  $SYM-H$  began. It is fair to assume that during the period of interest the magnetopause and tail currents sharply increased in the magnetosphere, and an intense asymmetric component of the ring current developed which was more than four times higher than the symmetric ring current component (167 and  $-37$  nT respectively).

On November 4 in the early hours of UT ( $\sim 09$ – $15$  LT), the effect of the eastward electrojet located south of this station was observed on Kotelny Island. This is evidenced by the positive bay in  $dH$ (ktn) and the negative bay in  $dZ$ (ktn) (see Figure 6). During this period there were no magnetic variations at the Zhigansk and Yakutsk stations. In  $\sim 8$  hours after the above isolated intense substorm, the following magnetic field disturbance began at these stations. In the magnetic field  $H$  component, from 6:50 UT both stations recorded a

gradual development of positive ( $dH$ (yak) $\sim 100$  nT,  $dH$ (zgn) $\sim 500$  nT) and negative bays ( $dH$ (yak)  $\sim -200$  nT,  $dH$ (zgn) $\sim -400$  nT) superimposed by oscillations with a period to several tens of minutes and an amplitude to 200 nT. The  $Z$  component at the Yakutsk station exhibits a change from the positive bay with  $dZ$ (yak) $\sim 300$  nT to the negative bay with  $dZ$ (yak) $\sim -200$  nT; and at the Zhigansk station, on the contrary, a change from the negative bay with  $dZ$ (zgn) $\sim -450$  nT to the positive one with  $dZ$ (zgn) $\sim 100$  nT. The magnetic field oscillations are also seen to be superimposed on the bays. On Kotelny Island, the  $dH$ (ktn) variations are similar to those at the Zhigansk station, but the  $dZ$ (ktn) variations are opposite. The disturbance ended at  $\sim 18$  UT, its total duration was  $\sim 11$  hrs. In the local time, the disturbance occurred in the afternoon, evening, and night hours from  $\sim 16$  to 03 LT of the next day.

The auroral indices on this day, as derived from [[https://wdc.kugi.kyoto-u.ac.jp/ae\\_realtime/](https://wdc.kugi.kyoto-u.ac.jp/ae_realtime/)], were  $AU \sim 500$ ,  $AL \sim -2000$  nT. In the sunlit hemisphere,  $SML$  and  $SMU$  are comparable and at some points in time amount to  $\pm 650$  nT [<https://supermag.jhuapl.edu/>], whereas in the nightside hemisphere  $SML$  of the westward electrojet ( $-2800$  nT) significantly exceeds  $SMU$  of the eastward electrojet (400 nT). The pattern of changes in the magnetic field  $H$  components at the Yakutsk stations, located in the dusk and night sectors during the development of the substorm, is consistent with the distribution of magnetic vectors of the global network SuperMag due to superposition of current systems DP2 and DP1 [Yakhnin, 2008]. The eastward electrojet took place in the afternoon and dusk sectors, as evidenced by the deviation signs of  $dH$  and  $dZ$ , at the latitude  $56^\circ < \Phi' < 61^\circ$ . In the late evening and night hours,

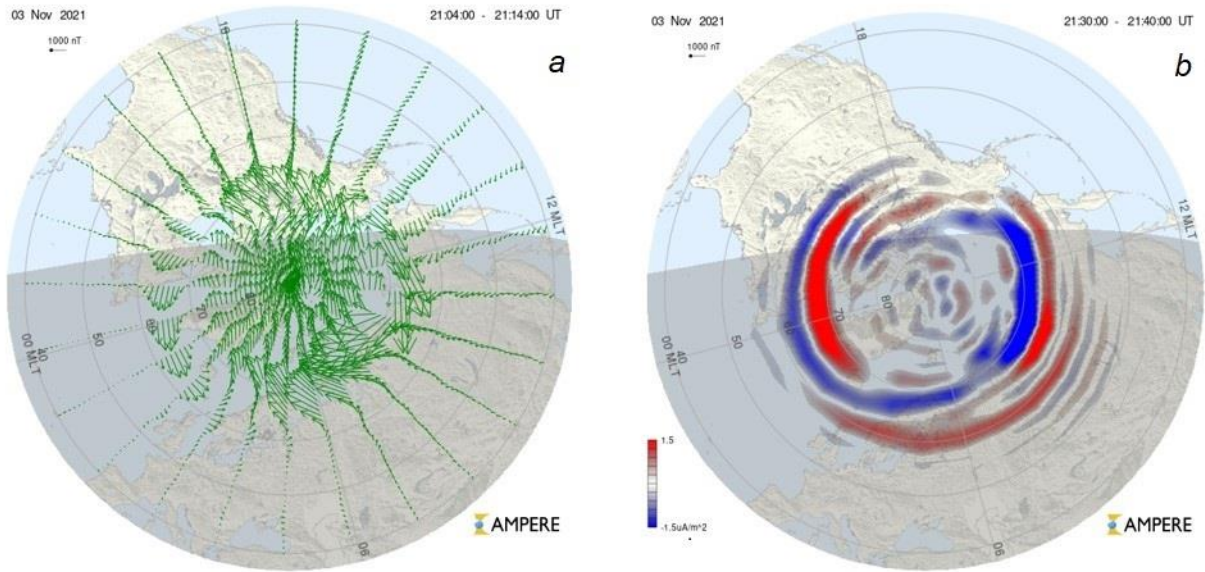


Figure 7. Distribution of horizontal magnetic vectors, rotated 90° clockwise (a) at ionospheric heights, and field-aligned currents (b) on November 3, 2021 at 21:04–21:14 UT (AMPERE calculations)

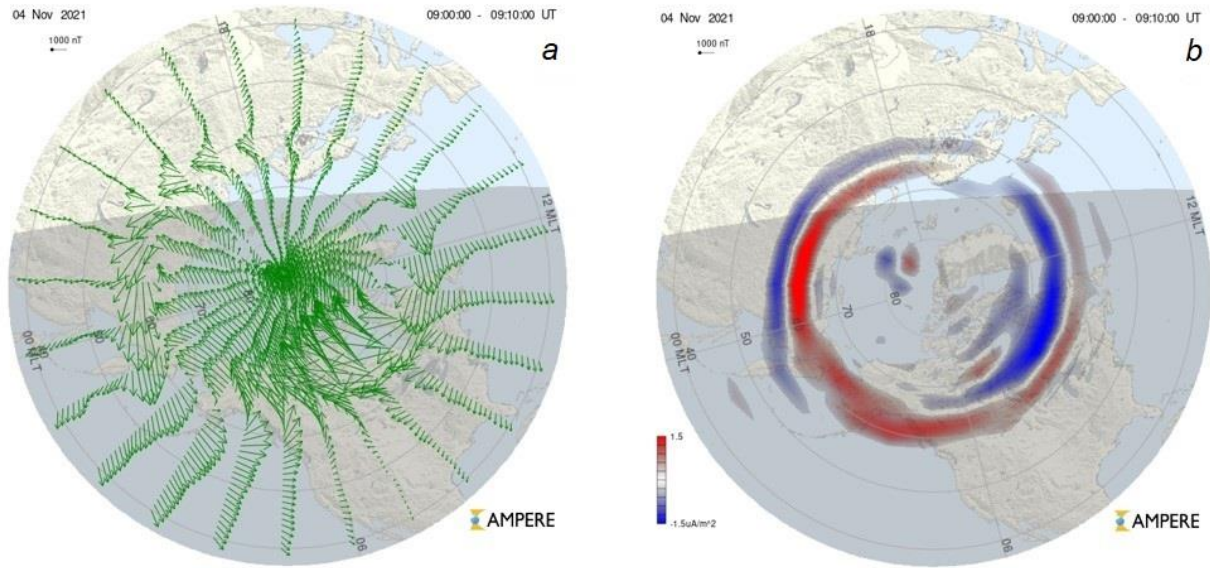


Figure 8. Distribution of horizontal magnetic vectors rotated 90° clockwise (a) at ionospheric heights and field-aligned currents (b) in the dusk sector on November 4, 2021 (AMPERE calculations)

the Zhigansk and Yakutsk stations were under a complex system of westward and eastward currents. Figure 8, similar to Figure 7, demonstrates the distribution of horizontal magnetic vectors in order to illustrate the direction of ionospheric equivalent currents and the distribution of field-aligned currents from AMPERE data [<https://ampere.jhuapl.edu/>] in the dusk sector. We can assume that in the dusk sector eastward currents do occur at the given latitudes (panel a); field-aligned currents flow into the ionosphere at  $\Phi' \sim 57^\circ\text{--}60^\circ$  and flow out of the ionosphere at  $\Phi' \sim 62^\circ\text{--}65^\circ$  (panel b). Based upon the pattern of field-aligned currents, it is expected that the center of gravity of the eastward electrojet is located at  $\Phi' \sim 58^\circ$ .

The *ASY-H* and *SYM-H* indices (see Figure 5, c, d) undergo changes indicating further development of the magnetic storm initial phase. The changes began on November 4 at  $\sim 00:45$  UT: there was a positive jump in *ASY-H* from 8 to 119 nT and a negative decrease in *SYM-H* from zero to  $-42$  nT at 01:27 UT. Then there was a decrease in *ASY-H* to 40 nT and an increase in *SYM-H* to  $-33$  nT at 02:47 UT. The observed changes in the indices manifested themselves in the magnetic field *H* component at the Yakutsk and Zhigansk stations as small negative bays deviated by  $\sim 46$  and  $\sim 60$  nT; on Kotelnny Island at that time a positive bay in *dH* (ktn) and a negative bay in *dZ* (ktn) began to develop.

Based upon variations in the ring current index *SMR* calculated from SuperMag data [<https://supermag.jhuapl.edu/>], we can conclude that the storm main phase

began at  $\sim 05:25$  UT and lasted until  $08:37$  UT, i.e. its duration was  $\sim 192$  min. The storm recovery phase lasted until November 11, was accompanied by the development of a number of substorms on November 5, 6, and 8–10 with  $AU < 200$  nT and  $AL > -400 \div -700$  nT.

The November 3 event, defined as an isolated intense substorm, is likely to be an element of the initial phase of the storm we describe. This can be inferred from *Dst* data [[https://wdc.kugi.kyoto-u.ac.jp/dst\\_provisional/index.html](https://wdc.kugi.kyoto-u.ac.jp/dst_provisional/index.html)] and variations in SW parameters. Figures 9, 10 illustrate changes in the interplanetary medium parameters on the days under study.

As it follows from Figure 10, the storm occurred against the background of positive IMF sector. SW and IMF varied from 19:00 UT on November 3 to November 10.

At first, they were detected in the solar plasma parameter  $\beta$ , which characterizes the ratio of thermal pressure to magnetic pressure, and its sharp increase from 1 to 5.9 was observed for 15 min (see Figure 9). Note [Kurazhkovskaya et al., 2021] that  $\beta$  is one of the important factors influencing the storm intensity — the lower  $\beta$  during the storm main phase, the greater its intensity. This pattern also manifested itself in the storm of interest: a maximum decrease in *SMR* was  $\sim -130$  nT. In the IMF parameters, there was a slight decrease in  $B$  from 2.6 to 1.5 nT at IMF zero north-south component, as well as decreases in the azimuthal component  $B_y$  from 2 to 1.4 nT and in the radial component  $B_x$  from  $-1$  to 0 nT (see Figure 10).

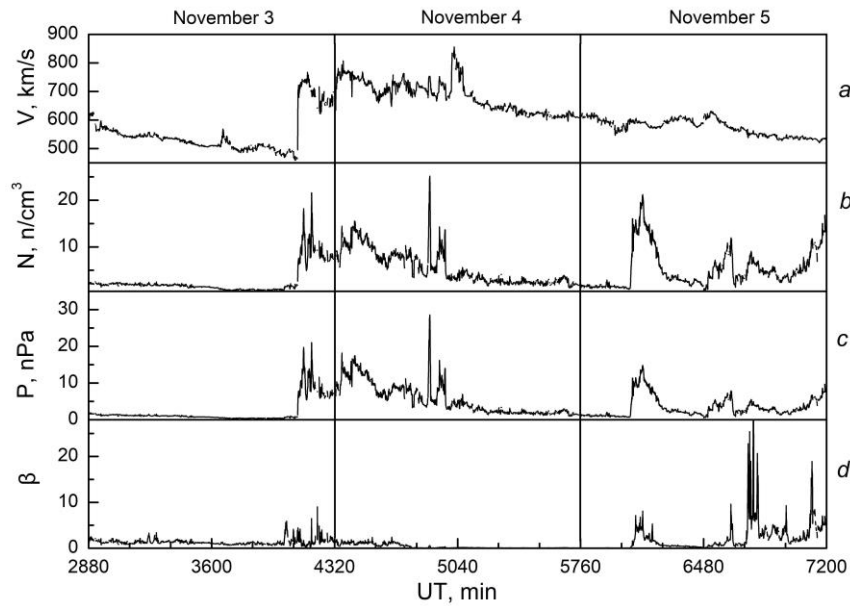


Figure 9. Changes in solar wind parameters on November 3–5, 2021: velocity  $V$  (a), proton density  $N$  (b), dynamic pressure  $P$  (c), parameter  $\beta$  — the ratio of thermal pressure to magnetic pressure (d)

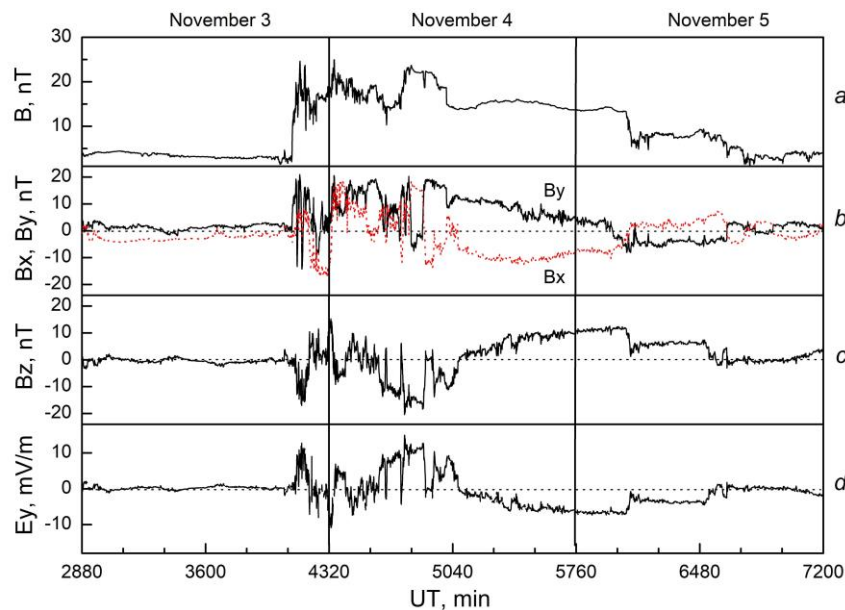


Figure 10. Changes in IMF  $B$  (a), its radial  $B_x$  and azimuthal  $B_y$  components (b), north-south component  $B_z$  (c), and SW azimuthal electric field  $E_u$  (d) on November 3–5, 2021

A sharp increase in the dynamic pressure  $P$  to  $\sim 7$  nPa occurred  $\sim 5$  min after the start of strong changes in  $\beta$ . Simultaneously, the SW velocity increased to  $\sim 700$  km/s; the density, to  $\sim 7$  cm $^{-3}$ ; IMF, to  $\sim 12$  nT; and strong fluctuations began in  $B_y$  and  $B_x$ , with  $B_z$  changing direction to the south 19 min after the sharp increase in  $P$ . At the same time, there was an abrupt rise in the SW azimuthal electric field  $E_y = -VB_z$  from zero in the positive direction to  $\sim 10$  mV/m and more.

During disturbances of the interplanetary parameters, interruption in the IMF sector structure was observed for  $\sim 15$  hrs. During this time,  $V$  increased from  $\sim 500$  to  $\sim 700$  km/s, reaching  $\sim 800$  km/s and higher during disturbances; and after the disturbances, the velocity of  $\sim 650$  km/s remained almost unchanged for more than 12 hrs. The IMF modulus was constant before the disturbances, 3 nT, then it increased sharply to 12 nT, being as high as  $\sim 25$  nT during the disturbances, and after them it was  $\sim 14$  nT for more than 12 hrs.

The magnetosphere did not respond strongly to the sharp increases in  $N$ ,  $P$ , and  $\beta$ , which occurred on November 5. This was manifested by weak changes in *ASY-H* and *SYM-H*, the horizontal  $H$  and vertical  $Z$  components of the magnetic field at the Yakutsk and Zhigansk stations (see Figure 6), as well as in auroral indices. This response of the magnetosphere may be explained by the northward IMF orientation, but this requires further investigation.

### VARIATIONS IN NATURAL ELECTRIC POTENTIALS AT THE YAKUTSK STATION AND THEIR RELATIONSHIP WITH MAGNETIC DISTURBANCES

It is of interest to comparatively analyze parameters of the magnetic field components and the electric potentials during the magnetic storm considered. Take a closer look at the behavior of natural potentials on November 3–4, 2021. Variations in one-hour *Dst* values during this storm are shown in Figure 4. Variations in the  $X$  and  $Y$  components were recorded with the geophysical instrument ADU-07 installed at the radiophysical station Oybenkel. Variations in natural potentials  $E$  were measured with the same instrument by underground non-polarizing electrodes spaced by 100 m [Kozlov et al., 2022].

The correlation coefficient of the difference between the natural potentials  $E_{NS}$ ,  $E_{EW}$  (north—south, east—west) and the corresponding magnetic components  $X$  and  $Y$  at 8:30 a.m. – 10:30 a.m.  $\rho(E_{NS}, B_y) = 0.69 \pm 0.1$  ( $p < 0.005$ ) and  $\rho(E_{EW}, B_x) = 0.88 \pm 0.1$  ( $p < 0.005$ ). The range of variation  $\rho = 0.5 \div 0.9$ . The relationship between variations in the natural potentials  $E_{EW}$  and their induced  $B_x$  variations can be expressed as  $E_{EW} = 0.05 B_x - 16$ , where  $E$  is measured in mV; and  $B$ , in relative units of ADU-07. It should be noted here that the shift in the expression obtained at  $B_x = 0$  varies from  $-12$  to  $-22$  during a storm due to the presence of slow components of variations that are superimposed by variations caused by faster pulsations. Accordingly, for  $E_{NS}$  and

$B_y$ , we obtain the relation  $E_{NS} = 0.06 B_y - 10$  when the shift changes from  $-6$  to  $-18$ .

Compare the measured variations in natural potentials during magnetic storms at the moments of maximum thawing of the seasonal thaw depth on September 7–8, 2017 and during the November 3–4, 2021 storm when the upper layer had already been freezing from above for a month, but the entire thaw depth had not yet frozen. During the two-step very strong G4-level storm on September 7–8, 2017 there were high-latitude geomagnetic variations accompanied by excitation of bursts (wave trains) of Pc5 geomagnetic pulsations.

During the first step, *Dst* ran to  $-142$  nT; and during the second step, to  $-124$  nT. The correlation coefficient of the difference between the natural potentials  $E_{NS}$ ,  $E_{EW}$  and the corresponding magnetic components  $X$  and  $Y$  during pulsations lasting for 8.33 hrs  $\rho(E_{NS}, B_y) = 0.77 \pm 0.1$  ( $p < 0.005$ ) and  $\rho(E_{EW}, B_x) = 0.65 \pm 0.1$  ( $p < 0.005$ ),  $\rho = 0.5 \div 0.9$ . The dependence of  $E_{NS}$  (mV/100 m) on the magnetic field strength (relative units of ADU-07e) during pulsations of the first burst (interval 5600–5700 s from the beginning of the day on September 8, 2017) can be expressed as  $E_{NS} = 0.0002 B_y - 22$ ; during the pulsations of the second burst (interval 40000–70000 s from the beginning of the day on September 8, 2017), as  $E_{NS} = 0.0002 B_y - 24$ . During the complete freezing of the top layer, which thaws in summer, (the January 26, 2021 storm), there were also high-latitude geomagnetic variations accompanied by excitation of bursts (wave trains) of Pc5 geomagnetic pulsations. It was a weak G1-level storm. During the storm, *Dst* was as high as 39 nT. The correlation coefficient between  $E_{NS}$ ,  $E_{EW}$  and  $B_x$ ,  $B_y$  during the pulsations  $\rho(E_{NS}, B_y) = 0.61 \pm 0.1$  ( $p < 0.005$ ) and  $\rho(E_{EW}, B_x) = 0.62 \pm 0.1$  ( $p < 0.005$ ). The dependence of  $E_{NS}$  (mV/100 m) on the magnetic field strength (relative units of ADU-07e) during pulsations at 16:50–17:00 UT can be expressed as  $E_{NS} = 0.0013 B_y - 27$ , and at 17:20–17:40 UT as  $E_{NS} = 0.0016 B_y - 28$ .

Thus, comparing the magnetic field components and the electric potentials during the above three magnetic storms occurring in different seasons (on maximum thawing of the active layer in September, on complete freezing of the active layer in late January and early November when the upper part of the active layer begins to freeze) allows us to conclude that with complete ground freezing there is a steeper dependence than with maximum thawing of the top layer of ground. The slope coefficient of the linear relationship is eight times higher. The coefficients of the dependence observed in early November 2021 are closer to winter ones. A change in the dependence coefficients is associated with a change in the conductivity of the active layer.

### GEOMAGNETIC STORM EFFECTS IN VLF EMISSION AMPLITUDE VARIATIONS

Observations of VLF emission amplitude variations carried out at the radiophysical station Oybenkel of SHICRA SB RAS in November 2021 have revealed a

wide variety of types of continuous and discrete natural radio noise in the range 1.0–7.0 kHz. Magnetic and electric components of VLF emission are recorded at the radio-physical station Oybenkel that is located at a distance of 25 km from man-made statics near Yakutsk and more than 5 km from the nearest power transmission line.

The work uses 1 s data on VLF noise received by an east-west oriented magnetic frame, amplified in a receiver-recorder, on 11 bandpass filters from 0.4 to 8.7 kHz, and converted by an analog-digital converter for storing in the recorder's memory [Murzaeva et al., 2001]. We have also employed data on VLF emission in a range to 20 kHz, received by a vertical electric asymmetric dipole.

Dynamic variations in VLF noise received by an east-west oriented magnetic frame during the November 3–4, 2021 storm are illustrated in Figure 11; their corresponding dynamic spectra in the range to 20 kHz received by the vertical electric asymmetric dipole are shown in Figures 12–15.

On the Earth surface, bursts of chorus waves and broadband hisses are generally observed during the development of magnetospheric substorms; VLF noise storms, during magnetic storms; and quasi-periodic VLF emissions, under quiet geomagnetic conditions [Manninen et al., 2020]. For the November 3–4, 2021 magnetic storm considered, there are both bursts of chorus waves and various quasi-periodic emissions, broadband and quasi-periodic hisses, various stimulated discrete and narrowband signals. When examining VLF emission variations during this period, we revealed the following chronology of events with manifestation of continuous and discrete emissions of various types:

1. VLF emission disturbances began with a burst of broadband hiss at 20:55:55 UT (see Figure 11). At first, the hisses were observed at 3.4–5.3 kHz, then the frequency range expanded to 3.0–5.7 kHz. With a gradual increase in the intensity of hisses, the upper limit of the range increased to 9 kHz at 21:20 UT. Then, at 21:40 UT, the hisses had a maximum intensity in the range 1.0–13.5 kHz. At 22:00 UT, the hisses began to weaken, the range became 2.0–6.0 kHz; and at the end of the hour, the hisses ceased abruptly. These continuous hisses in various frequency ranges over the period from ~21 to 23 UT manifested themselves in VLF emissions when IMF  $B_z$  began to change direction from south to north (from minimum negative to maximum positive values).

2. From ~22:30 on November 3 to 02:00 UT on November 4, 2021, chorus waves (0.1–0.3 s discrete elements with increasing frequency) were recorded in VLF emission. The frequency range of the chorus waves varied from 1.5–8.0 kHz to 3.0–5.0 kHz. At the same time there were 2–3 s quasi-periodic structures with choral elements that lasted from 23:00 on November 3 to 01:20 UT on November 4, 2021. In the same time period, whistling atmospheric (whistlers) were detected which stimulated short discrete signals (see Figure 12).

3. From 01:00 to 03:00 UT on November 4, 2021, VLF emissions of various types were recorded. First, 0.7–4.5 kHz hisses with a maximum intensity in two frequency bands 1.3–3.2 and 3.5–5.0 kHz (see Figure 13). At this time, IMF  $B_z$ , as well as for the time period 21:00–23:00 UT on November 3, 2021, changed from minimum negative values to positive ones.

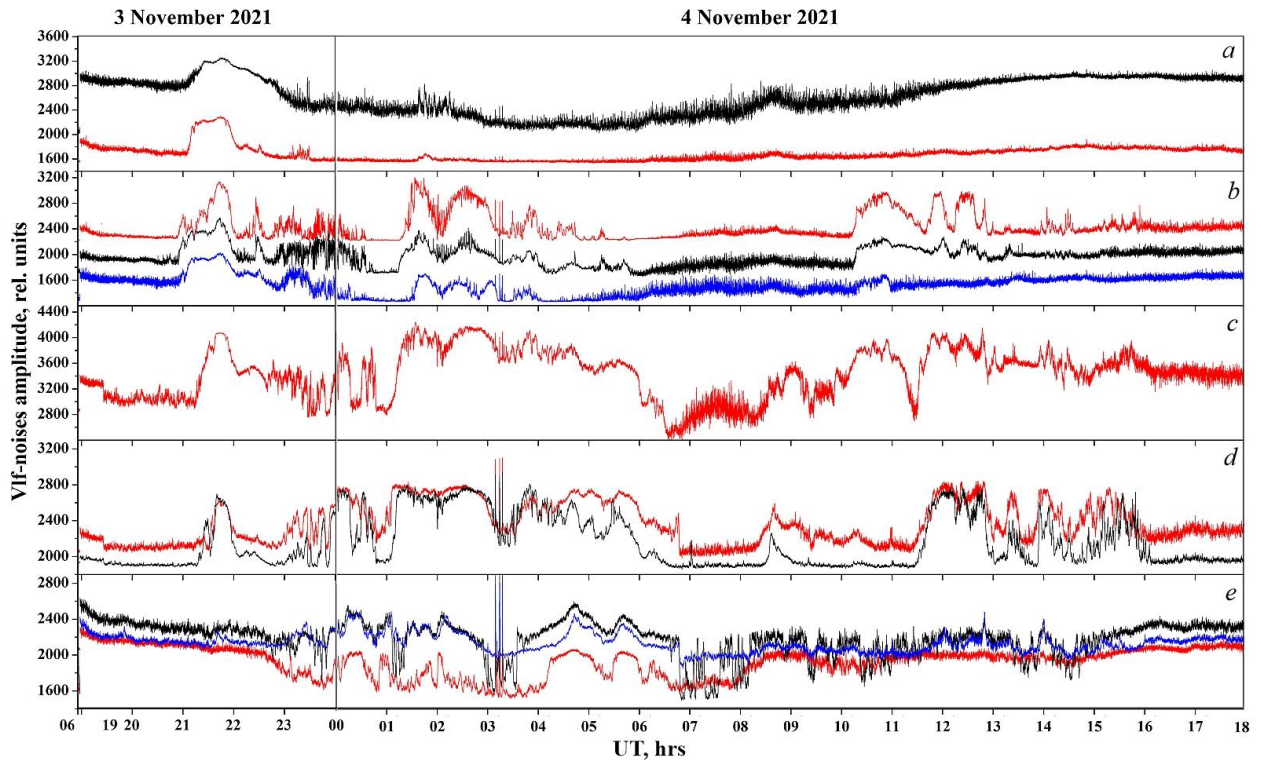


Figure 11. Variations in the amplitude of VLF noise received on November 3–4, 2021 by an east-west oriented magnetic frame: black — 8.7 kHz, red — 6.7 kHz (a); blue — 5.6 kHz, black — 4.0 kHz, red — 3.1 kHz (b); red — 2.2 kHz (c); black — 1.6 kHz, red — 1.1 kHz (d); blue — 0.8 kHz, black — 0.6 kHz, red — 0.4 kHz (e)

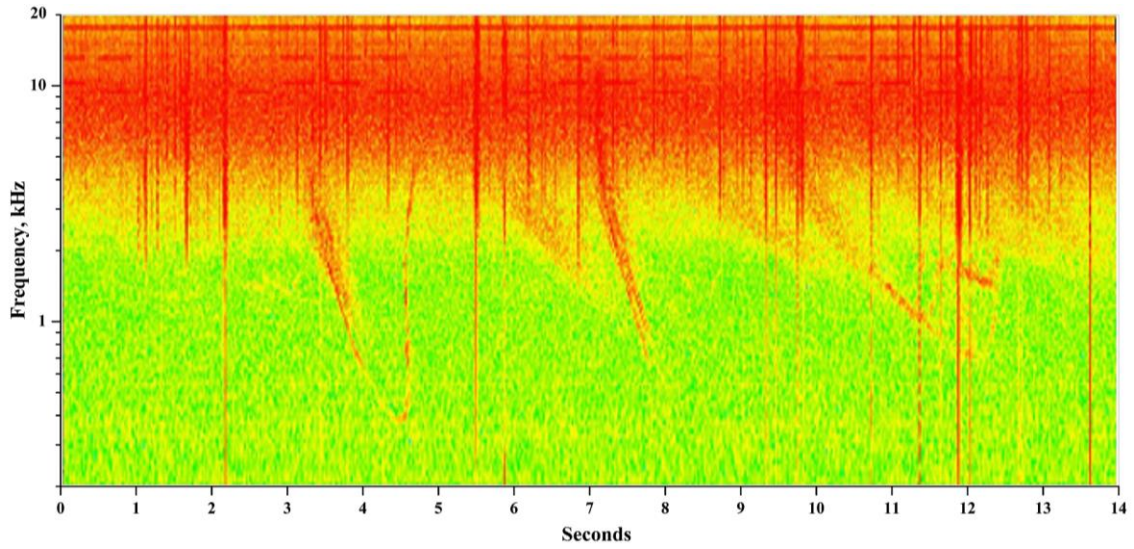


Figure 12. Dynamic spectra in a range to 20.0 kHz on November 3, 2021 at 23:00:00–23:00:14 UT: whistling atmospherics that stimulate triggering emission

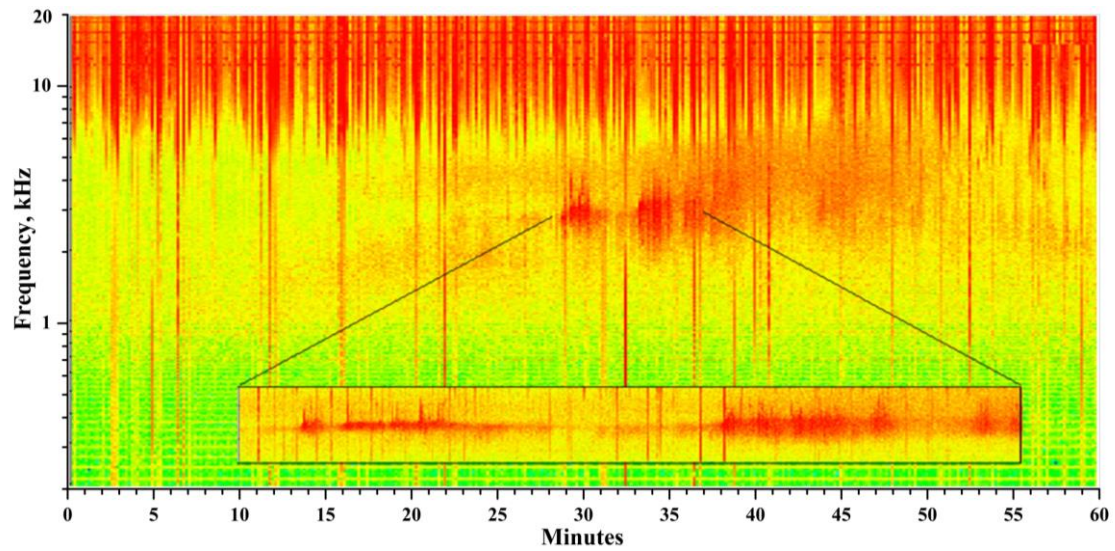


Figure 13. Dynamic spectrum of VLF emission in a range to 20.0 kHz at 01:00 UT on November 4, 2021. The embedded panel shows a narrowband hiss at frequencies 2.5–3.5 kHz, which generates trigger signals and chorus waves

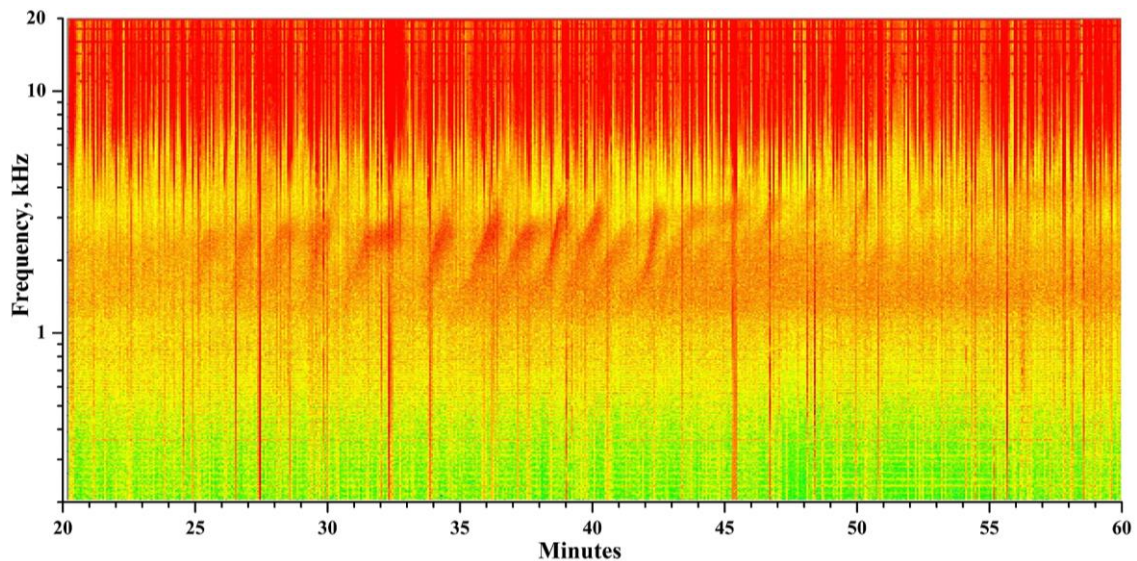


Figure 14. QP hisses at frequencies 1.5–5.0 kHz on November 4, 2021 at 02:00–03:00 UT. On the time scale are minutes from the top of the hour

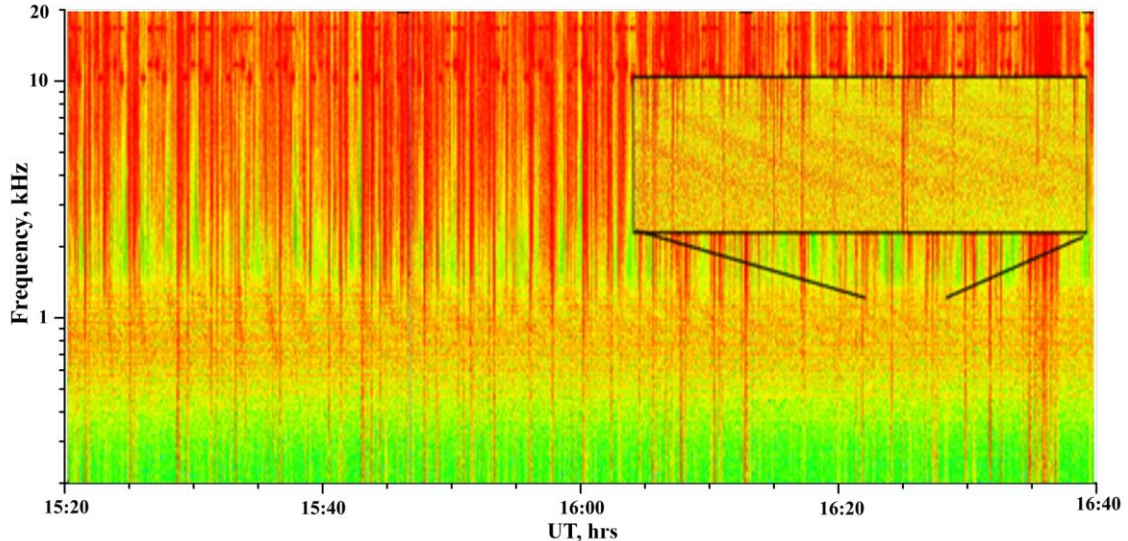


Figure 15. Quasi-periodic whistler-generated emissions against the background of hiss at 3.0–5.0 kHz on November 4, 2021

In addition, narrow-band hisses were observed at frequencies 2.3–2.8, 2.6, 2.5–3.0, 2.0–5.0 kHz, which occurred with stimulation of discrete trigger signals and chorus waves (embedded panel in Figure 13). At the same time, 2–3 s quasi-periodic hisses induced by whistlers at 3.5–4.5 and 3.2–5.0 kHz were observed against the background of the continuous hiss (see Figure 12). Duration of these quasi-periodic hisses was almost 2 min. At the same time, chorus waves were observed at 2.3–5.0, 2.0–4.5, and 1.5–5.0 kHz. From 02:15 to 02:50 UT, quasi-periodic (QP) hisses were recorded with increasing frequencies in the range 1.6–4.3 kHz with 80–100 s periods (see Figure 14). At that time, IMF  $B_z$  was positive. Note also that at 03:40–04:00 UT a hiss was detected at 1.3–2.7 kHz and chorus waves occurred.

4. Throughout the time interval of interest, a weak plasmaspheric hiss was observed at 0.6–3.0 kHz with periodic slight increases and decreases in intensity with a maximum from 04:00 to 09:00 UT on November 4, 2021 when no other VLF emission types were detected.

5. On November 4, 2021 from 10:10 to 11:40 UT, there was a broadband hiss at different frequencies in the range 2.2–5.0 kHz with a maximum intensity at 10:50 UT within 2.2–4.8 kHz. During this period,  $B_z > 0$ , and the expansion of the frequency range and its subsequent narrowing are associated with a change from  $B_z < 0$  to  $B_z > 0$ , and vice versa. Broadband hisses of 3.0–5.2 kHz were also recorded from 11:50 to 12:50 UT. During this period,  $B_z$  changed its values from negative to positive. These hisses were accompanied by 3.0–5.0 kHz quasi-periodic emissions generated by whistlers (see Figure 15). At 12 UT on November 4, intense continuous chorus waves were recorded at 1.0–1.5, 1.7–2.7, 3.2–4.4, 1.4–4.4, 0.9–3.5 kHz. Besides, there were 3 s narrowband hisses at 4.4 kHz, as well as 2–3 s quasi-periodic structures with choral elements at 1.9–2.9 and 0.8–1.4 kHz, which lasted from 12:10 to 13:10 UT.

6. From 13:10 UT, the VLF emission disturbances weakened. The most notable events during this time were chorus waves and narrowband hisses at 5.5 kHz,

which were driven by whistlers from 13:50 to 14:10 UT. At 15:20–16:00 UT, there were 2–4 s intense narrowband hisses at 1.0–4.0 kHz, accompanied by choral elements. After 16:00 UT, the VLF emission intensity recovered to the level corresponding to that observed before the onset of the storm.

Thus, noteworthy among the main events are continuous and quasi-periodic broadband hisses associated with the change of  $B_z$  direction:

Broadband hisses with changes in the lower and upper frequencies and the VLF emission intensity, which correspond to changes of the values and direction of  $B_z$  relative to the geomagnetic field from south to north (from negative to positive values). Such broadband hisses were recorded in the ranges 1.0–13.5 kHz at 21:00–23:00 UT on November 3, 0.7–4.5 kHz at 01:00–03:00 UT on November 4, and 3.0–5.2 kHz at 12:00–13:00 UT on November 4.

- Broadband hiss at 2.2–5.0 kHz on November 4 at 10:10–11:40 UT. At this time,  $B_z > 0$ , and the expansion of the frequency range and its subsequent narrowing is attributed to the change from  $B_z < 0$  to  $B_z > 0$ , and vice versa.
- QP hisses on November 4, 2021 at 02:15–02:50 UT with an increase in frequencies in the range 1.6–4.3 kHz with 80–100 s periods;  $B_z > 0$ .

### EFFECTS OF SOLAR FLARES IN VLF EMISSION AMPLITUDE VARIATIONS AND PHASE VARIATIONS OF SIGNALS FROM VLF RADIO STATIONS

The Yakutsk station (62.02° N, 129.70° E) and the Polar Geocosmophysical Observatory Tixie Bay (71.6° N, 128.9° E) record radio signals in a very low-frequency band (VLF — 3–30 kHz).

An increase in the X-ray flux during solar flares leads to a sharp increase in the electron density in the ionosphere. This causes sudden phase and amplitude anomalies (SPA, SAA) during propagation of electro-

magnetic VLF and LF signals. A decrease in the phase delay in the VLF radio signal during SPA can be interpreted as a decrease in the effective height of the Earth—lower ionosphere waveguide, and a decrease in damping of radio waves (an increase in the amplitude of the recorded signal) during SAA when propagating in the waveguide can be interpreted as a decrease in the vertical electron density gradient of the lower ionosphere [Kumar, Kumar, 2018].

In diurnal amplitude and phase variations of radio signals from transmitters NAA (USA, 44.65° N, 67.28° W, 24.0 kHz signal frequency), NWC (Australia, 21.82° S, 114.17° E, 19.8 kHz), and Khabarovsk (RSDN-20, 11.904 kHz) when recorded at the Yakutsk and Tixie Bay stations due to an M1.7 X-ray flare on November 2, 2021, the maximum intensity of the X-ray flux was detected at 03:01 UT. A maximum amplitude increase during SAA was 1.69 (03:09 UT) and 2.59 dB (03:09 UT) along the NAA—Tixie Bay and NAA—Yakutsk radio paths respectively. Along the NWC—Yakutsk radio path, the maximum amplitude during SAA was 1.53 dB (03:09 UT), and a decrease in the phase delay in radio signal during SPA was 90° (03:09 UT). Along the Khabarovsk—Yakutsk radio path, a maximum amplitude increase during SAA was 1.18 dB (03:04 UT), and a decrease in the phase delay in radio signal during SPA was 16° (03:09 UT). Along the Khabarovsk—Tixie Bay radio path, the maximum amplitude increase during SAA was 2 dB (03:04 UT), and a decrease in the phase delay in radio signal

during SPA was 21° (03:09 UT).

Information on solar X-ray flares of class C2.9 and higher from October 26 to November 2, 2021 and on SAA of radio signals from RSDN-20 (11.904 kHz), NWC (19.8 kHz), and NAA (24 kHz) transmitters recorded at the Yakutsk and Tixie Bay stations is presented in Table 1. The catalog of solar flares of class C2.9 and higher from October 26 to November 2, 2021 and SPA of radio signals from RSDN-20 (11.904 kHz) and NWC (19.8 kHz) transmitters, detected at the Yakutsk and Tixie Bay stations is given in Table 2. The recorded SPA values are reduced to unit length of radio paths (degree/Mm).

Note that on October 26 from 20:47 UT, the RSDN-20 transmitters were turned off until 08:03 UT on October 29, 2021; on November 1, the NWC transmitter was turned off from 00:00 to 06:40 UT.

Represent the maximum amplitude change during SAA as a function of maximum X-ray flux  $P$  in the range 1–8 Å and averaged along the entire radio path of the cosine of the solar zenith angle  $X$ . The zenith angle values along the paths with coordinates at a resolution of 200 km were calculated by the algorithm [http://stjarnhimlen.se/comp/tutorial.html]. Along the Novosibirsk—Yakutsk radio path, with increasing X-ray flux of solar flares the amplitude increases relative to background (undisturbed) values. Along the Khabarovsk—Yakutsk and NWC—Yakutsk radio paths, saturation is recorded when the flux runs to  $6 \cdot 10^{-6} \text{ W/m}^2$ .

Table 1

Solar X-ray flares from October 26 to November 2, 2021 and sudden amplitude anomalies in radio signals from RSDN-20 (11.904 kHz), NWC, and NAA transmitters

Date	Time of maximum X-rays	Class	Khabarovsk RSDN-20, dB		Novosibirsk RSDN-20, dB		Krasnodar RSDN-20, dB		NWC, dB	NAA, dB	
			Yakutsk	Tixie	Yakutsk	Tixie	Yakutsk	Tixie		Yakutsk	Yakutsk
Oct. 26, 2021	1:04	C9.3	1.04	–	0.9	–	night	night	3.42	3.17	–
Oct. 26, 2021	1:50	C3.5	0.45	–	1.5	–	night	night	0.82	–	–
Oct. 26, 2021	2:47	M1.3	0.57	–	3.96	–	1.47	–	1.98	2.64	–
Oct. 26, 2021	6:04	C7.8	0.57	–	1.06	–	1.71	–	1.26	1.31	–
Oct. 27, 2021	6:08	C8.5	off	off	off	off	off	off	1.47	1.1	–
Oct. 28, 2021	7:40	M1.4	off	off	off	off	off	off	2.32	1.28	night
Oct. 29, 2021	2:42	M1.5	off	off	off	off	off	off	2.9	2.07	1.24
Oct. 29, 2021	5:58	C4.8	off	off	off	off	off	off	–	1.66	1.16
Oct. 29, 2021	6:07	C5.9	off	off	off	off	off	off	1.12	–	1.69
Oct. 30, 2021	3:15	C3.9	0.59	–	–	–	–	–	–	–	–
Oct. 31, 2021	7:06	C2.9	–	–	0.48	–	–	–	–	–	–
Nov. 01, 2021	1:45	M1.5	1.71	1.01	1.8	–	night	night	off	3.61	1.78
Nov. 02, 2021	3:01	M1.7	1.18	2	2.78	–	–	–	1.53	2.59	1.69

Table 2

Solar X-ray flares from October 26 to November 2, 2021  
and sudden phase anomalies of radio signals from RSDN-20 (11.904 kHz) and NWC transmitters

Date	Time of maximum X-rays	Flare class	Khabarovsk RSDN-20, deg./Mm		Novosibirsk RSDN-20, deg./Mm		Krasnodar RSDN-20, deg./Mm		NWC, deg./Mm
			Yakutsk	Tixie	Yakutsk	Tixie	Yakutsk	Tixie	Yakutsk
Oct. 26, 2021	1:04	C9.3	5.5	–	–	–	night	night	–
Oct. 26, 2021	1:50	C3.5	–	–	–	–	night	night	–
Oct. 26, 2021	2:47	M1.3	7.5	–	3.03	–	–	–	–
Oct. 26, 2021	6:04	C7.8	1.43	–	1.33	–	1.65	–	–
Oct. 26, 2021	9:52	C5.0	night	night	night	night	1.15	–	night
Oct. 27, 2021	6:08	C8.5	off	off	off	off	off	off	5.85
Oct. 28, 2021	7:40	M1.4	off	off	off	off	off	off	8.62
Oct. 29, 2021	2:42	M1.5	off	off	off	off	off	off	11.7
Oct. 29, 2021	5:58	C4.8	off	off	off	off	off	off	–
Oct. 29, 2021	6:07	C5.9	off	off	off	off	off	off	5.96
Oct. 30, 2021	3:15	C3.9	3.14	–	–	–	–	–	2.34
Oct. 31, 2021	7:06	C2.9	–	–	1.89	–	–	–	–
Nov. 01, 2021	1:45	M1.5	8.29	5.76	4.17	–	night	night	off
Nov. 02, 2021	3:01	M1.7	11.43	8.64	–	–	–	–	9.57

With a further increase in the ionizing X-ray flux, the signal amplitude increase reduces. Similar changes in SAA are discussed in other works (e.g., [Todoroki et al., 2007]). To describe the dependence of SPA on X-ray flux and solar zenith angle, we make use of the empirical expression [Orlov, 1998]

$$\Phi = A + B \lg(P \cos(X)), \quad (1)$$

where  $\Phi$  is a change in signal phase relative to the undisturbed value, reduced to unit length of the radio path;  $P$  is the maximum intensity of solar X-ray flux in the range 1–8 Å during a flare, and  $\cos X$  is the cosine of the

solar zenith angle averaged throughout the radio path. From the data on SPA (see Table 2), the algorithm [<http://stjarnhimlen.se/comp/tutorial.html>] was used to determine the solar zenith angle  $X$  from geographic coordinates along each of the radio paths with a step of 200 km. We assumed the conditions for radio signal propagation to be nighttime when  $\cos X < 0$ . Table 3 lists the parameters of model (1) estimated by the least square method for the Khabarovsk—Yakutsk, Novosibirsk—Yakutsk, and NWC—Yakutsk radio paths.

Table 3

Parameters of SPA dependence on the logarithm of the product of X-ray flux [1–8 Å] by the solar zenith angle cosine averaged along a propagation path

Radio path, length	Sample size	Coefficient A	Coefficient B	Determination coefficient $R^2$	Standard deviation of residuals, deg./Mm
Khabarovsk—Yakutsk, 1.40 Mm	6	74.56±12.3	12.36±2.22	0.89	1.37
Novosibirsk—Yakutsk, 2.64 Mm	4	9.68±14.66	1.22±2.51	0.1	1.46
NWC—Yakutsk, 9.40 Mm	6	67.64±15.99	11.51±3.05	0.78	1.73

The low coefficients of model (1) with large fluctuations, as well as the small coefficient of determination, were obtained under the conditions of SPA recording along the Novosibirsk (RSDN-20) — Yakutsk path due to the small sample size, with flares on October 26 (see Table 2) of classes M1.3 and C7.8 having an increased X-ray background, which reduced the sensitivity of SPA. The SPA data acquired along the Khabarovsk (RSDN-20) — Yakutsk and NWC—Yakutsk radio paths from October 26 to November 2, 2021 is well described by the linear dependence on the logarithm of the product of X-ray flux 1–8 Å by zenith angle cosine averaged along the propagation path. The estimates of model (1) do not contradict those we have obtained earlier for a larger sample size [Starodubtsev et al., 2019].

To determine how the effective height  $\Delta h$  of the Earth—ionosphere waveguide change from the recorded phase delay in VLF radio signal at SPA under conditions of single-mode propagation, we employ the expression [Mitra, 1977]

$$\Delta\varphi = \frac{360d}{\lambda} \left( \frac{1}{2R} + \frac{\lambda^2}{16h_n^3} \right) \Delta h, \quad (2)$$

where  $\Delta\varphi$  is a change in VLF radio signal phase at SPA (degrees);  $R$  is the Earth radius (km);  $\lambda$  is the wavelength (km);  $d$  is the length of the radio path (km);  $h_n$  is the medium height of the ionosphere (70–74 km).

In our calculations, we took  $h_n=72$  km. The Earth radius was determined on each radio path by averaging the values found from latitudes corresponding to the path sections with the step of 200 km, using the reference ellipsoid

model WGS 84 [<https://planetcalc.ru/7721/?thanks=1>]. Changes in the effective height of the Earth—ionosphere waveguide, estimated from phase changes in radio signals from the RSDN-20 (11.904 kHz) and NWC (19.8 kHz) radio transmitters recorded at the Yakutsk and Tixie Bay stations during SPA from October 26 to November 2, 2021, are presented in Table 4.

Figure 16 illustrates changes in the effective height of the Earth—ionosphere waveguide along the NWC—Yakutsk and Khabarovsk—Yakutsk radio paths depending on  $P\cos(X)$ .

A greater change in the height of the waveguide ( $\approx 1$  km) is observed on the mid-latitude radio path Khabarovsk—Yakutsk relative to the NWC—Yakutsk path, half of which is located at low latitudes and crosses the geomagnetic equator. This change may be linked to the manifestation of the equatorial ionospheric anomaly.

Analysis of amplitude-phase variations recorded during sudden ionospheric disturbances on October 26 – November 2 has shown that the VLF radio signal propagation at 11.904 kHz along the meridian under daytime conditions on the 1400 km path can be considered single-mode. In the network of long radio paths that were found to be in night conditions, this fact may be useful in increasing the sample size of recorded SAA and SPA. We have adopted the parameters of the SPA model that is satisfactorily described by the linear function  $\lg(P\cos X)$ . This can be used for estimating the X-ray flux during solar flares by the surface method. We have estimated the change in the effective height of the Earth—ionosphere waveguide from recorded SPAs.

Table 4

Changes in the effective height of the Earth—ionosphere waveguide, estimated by phase changes of RSDN-20 (11.904 kHz) and NWC (19.8 kHz) radio signals, recorded at the Yakutsk and Tixie Bay stations during SPA on October 26 – November 2, 2021

Date	Time of maximum X-rays	Flare class	Khabarovsk RSDN-20, km		Novosibirsk RSDN-20, km	Krasnodar RSDN-20, km		NWC, km
			Yakutsk	Tixie	Yakutsk	Yakutsk	Yakutsk	
Oct. 26, 2021	1:04	C9.3	2.08	–	–	night		–
Oct. 26, 2021	2:47	M1.3	2.84	–	1.15	–		–
Oct. 26, 2021	6:04	C7.8	0.54	–	0.5	0.62		–
Oct. 26, 2021	9:52	C5.0	night	night	night	0.43		night
Oct. 27, 2021	6:08	C8.5	off	off	off	off		2.11
Oct. 28, 2021	7:40	M1.4	off	off	off	off		3.1
Oct. 29, 2021	2:42	M1.5	off	off	off	off		4.21
Oct. 29, 2021	6:07	C5.9	off	off	off	off		2.15
Oct. 30, 2021	3:15	C3.9	1.19	–	–	–		0.84
Oct. 31, 2021	7:06	C2.9	–	–	0.72	–		–
Nov. 01, 2021	1:45	M1.5	3.14	2.18	1.58	night		off
Nov. 02, 2021	3:01	M1.7	4.33	3.27	–	–		3.45

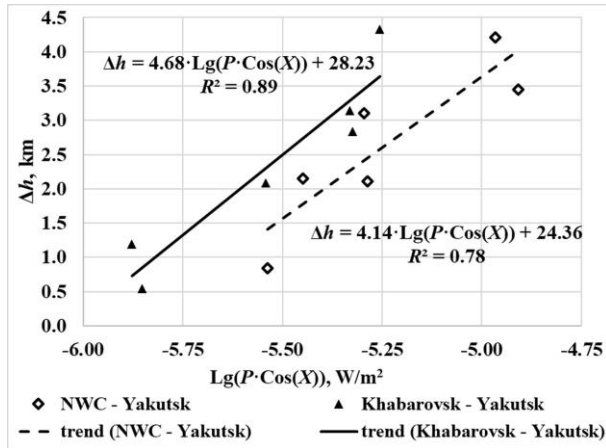


Figure 16. Changes in the effective height of the Earth—ionosphere waveguide on the NWC — Yakutsk and Khabarovsk — Yakutsk radio paths depending on solar X-rays

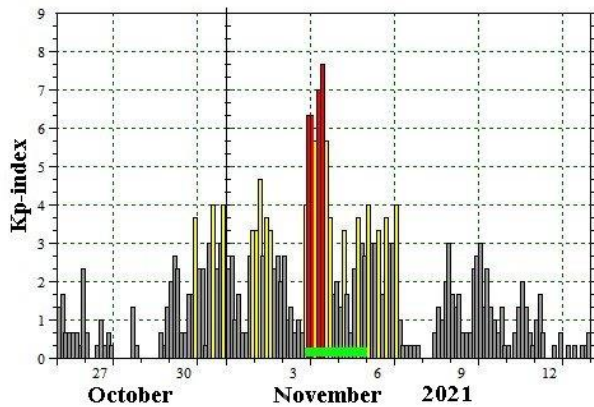


Figure 17. Geomagnetic conditions according to  $K_p$  on October 26 – November 13, 2021. The green rectangle marks the Forbush effect

### IONOSPHERIC CONDITIONS DURING FORBUSH EFFECT AS OBSERVED AT THE ZHIGANSK STATION

Figure 17 illustrates variations in the three-hour planetary geomagnetic activity index  $K_p$  on October 26 – November 13, 2021 before and after the Forbush effect. The period of interest was mostly quiet and moderately disturbed except for November 3–4 when  $K_p > 6$  with a maximum of 8– (highlighted in red).

The digisond or digital ionospheric station DPS-4 at the Zhigansk station ( $\Phi'61^\circ$  N,  $\Lambda'194^\circ$  E) probes the ionosphere at 1–12 MHz frequencies in a patrol mode every 15 min. Figure 18 shows hourly critical frequencies  $f_oF2$  of the ionospheric F2 layer for November 1–9, 2021. The Forbush effect, or a decrease in the intensity of galactic cosmic rays, was detected on November 3–5, 2021 (green rectangle, see also Figure 2).

It can be seen that after the onset of the Forbush effect, namely, during its recovery phase, complete absorption and shielding of HF radio waves were observed in the ionosphere (conditions B and A are marked with a gray rectangle) for ~12 hrs. Recall that under condition B the

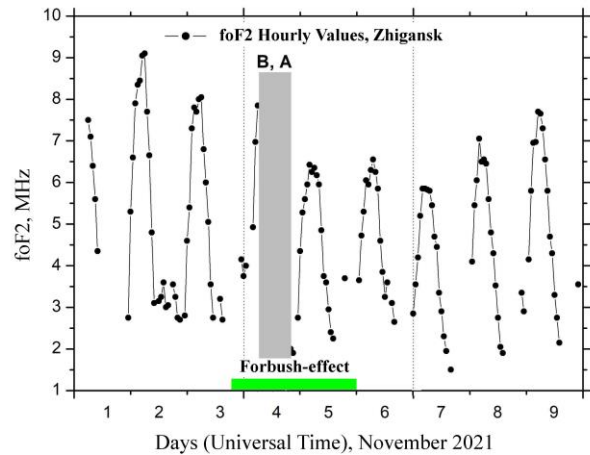


Figure 18. Hourly variations in  $f_oF2$  at the ionospheric station Zhigansk on November 1–9, 2021. Total absorption and shielding of HF radio waves; the gray rectangle denotes conditions B, A

measurement is affected or precluded by complete absorption of radio waves; and under condition A, by the presence of an underlying layer (shielding) [URSI Manual..., 1977]. Note also that the aforementioned ionospheric conditions were not observed during the recovery phase of the Forbush effect.

Figure 19 is similar to Figure 18, but  $f_oF2$  variations (light circles) are shown for four days per each sounding session. It can be seen that the decrease in  $f_oF2$  from 8 to 4 MHz began at about 07:00 UT on November 4 (16:00 LT) and was observed for ~30 min. This clearly indicates a shift in the boundary of closed field lines toward the equator or the development of magnetospheric-ionospheric disturbance. The event occurred before the beginning of the F2-layer absorption and shielding period that lasted for ~14 hrs. Thus, the delay in ionospheric disturbances at the latitude of the Zhigansk station (conditions B, A) from the beginning of the Forbush effect was ~7 hrs.

Figure 20 illustrates riometric absorption variations at the station Maimaga on November 3–5, 2021. The green segment represents the Forbush effect; the blue one, ionospheric disturbances or conditions B, A over the Zhigansk station. It can be seen that the onset of the Forbush effect in riometric absorption variations at the end of November 3 was marked by a short-term increase in intensity to 0.75 dB, which suggests the arrival of a shock wave from a solar flare to Earth's magnetopause. Then, until ~08:00 UT on November 4, there are gaps in data on riometric absorption variations. Absorption maxima to 2.5 dB are observed during ionospheric disturbances.

Using data from the ionospheric station Zhigansk, we found that during the first half of the Forbush effect there was an ionospheric disturbance that manifested itself in complete absorption and shielding of HF radio waves.

After the active phase of the Forbush effect, the ionospheric station Zhigansk observed  $f_oF2$  lowered by 1.5–2.0 MHz due to the magnetospheric-ionospheric storm accompanying the Forbush effect.

Riometric absorption suggests that absorption maxima are recorded during the Forbush-effect decrease.

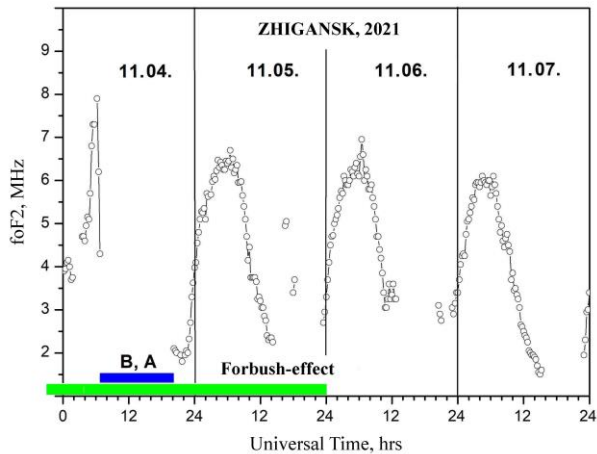


Figure 19. Fifteen-minute variations in  $f_oF_2$  at the ionospheric station Zhigansk on November 4–7, 2021. Total absorption and shielding of HF radio waves; the blue rectangle indicates conditions B, A

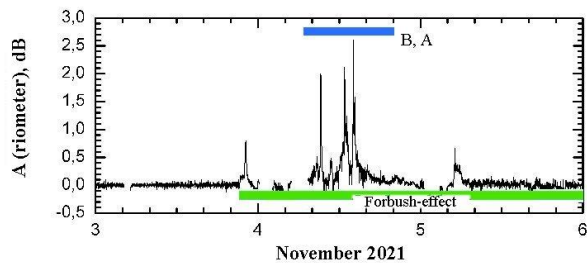


Figure 20. Riometric absorption variations on November 3–5, 2021. Total absorption and shielding of HF radio waves; the blue rectangle marks conditions B, A; the green one, time of the Forbush effect

## OPTICAL OBSERVATIONS

The SHICRA SB RAS meridional network of optical stations consists of three observation stations. Three identical spectrographs are installed at the optical stations Tixie Bay, Maimaga (63° N, 129.5° E, near Yakutsk), and Neryungri (56.7° N, 124.7° E) that are spaced in latitude.

Since 2014, permanent recording of hydroxyl bands OH(3, 1) has been carried out at the optical station Maimaga that is located 120 km north of Yakutsk. The infrared spectrograph detects OH(3, 1) bands in the far infrared region ( $\sim 1.5 \mu\text{m}$ ). It consists of a Shamrock monochromator equipped with a highly sensitive infrared photodiode detector manufactured by Andor Technology. The operating wavelength range is 1490–1544 nm, cooling is  $-60^\circ\text{C}$ , the opening angle is  $\sim 3^\circ$ , and the resolution of the spectrograph with an entrance slit 0.2 mm wide is 0.8 nm. Spectra of OH(3, 1), emitted at an altitude of  $\sim 87$  km, are recorded automatically at a solar depression angle  $>9^\circ$  every minute and transmitted daily to the Institute's server.

In September 2015, a similar infrared spectrograph was installed at the Polar Geocosmophysical Observatory (PGO) Tixie Bay; and in October 2017, at the observation station Neryungri. Thus, all three stations have identical photosensitive infrared spectrographs

that detect the hydroxyl band in the far infrared region. According to many recent works, the OH(3, 1) band is thermalized quite well [Shefov et al., 2006] and corresponds to the ambient temperature of the neutral atmosphere at the height of its emission. The choice of the hydroxyl emission band in the infrared region is due to three circumstances: firstly, the highest intensity of hydroxyl emissions in this spectral region; secondly, the lower contribution of parasitic light from stars and the Moon; and thirdly, the absence of auroral emissions.

Measurements with the infrared spectrograph were made at night in cloudless and slightly overcast weather. There were OH(3, 1) emissions recorded with an exposure of 60 s. The method of estimating the rotational temperature of molecular emissions is based on fitting model spectra, constructed taking into account the instrumental function of the device for different predetermined temperatures to the actually measured spectrum, by the least square method.

No significant variations in the neutral atmosphere temperature beyond the noise level were detected during GLE and Forbush decreases. Observations on the temperature of the neutral atmosphere at an altitude of  $\sim 87$  km for October 11 – November 20, 2021 from the stations Neryungri, Maimaga, and Tixie Bay are shown in Figure 21.

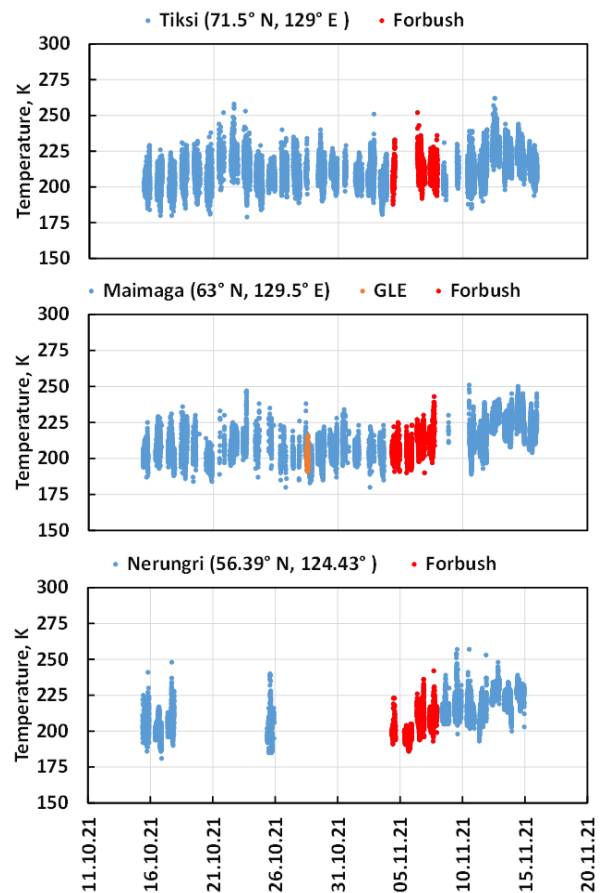


Figure 21. Rotational temperatures of OH(3, 1) emission at three different stations

## OBSERVATIONS OF AURORAS AND SUBAURORAL GLOW ON THE MERIDIAN OF YAKUTSK DURING THE NOVEMBER 4, 2021 MAGNETIC STORM

The magnetic storm main phase began on November 3, 2021 at ~21:35 UT due to arrival of plasma flow from a solar flare. Optical observations at the Maimaga and Tixie Bay stations were performed using the astronomical program until 21:20 UT on November 3 and were automatically continued on November 4 from 08:50 and 09:15 UT respectively. The beginning of observations at the Maimaga station was characterized by intermittent clouds, and only from ~09:15 to ~11:00 UT did the transparency of the atmosphere become satisfactory for recording auroras and subauroral glow throughout the sky. Due to atmospheric conditions, auroral dynamics could be recorded by the Tixie Bay station until ~11:00 UT.

Auroras at the Tixie Bay station were observed by the all-sky camera Keo Horizon in the visible region. At

the Maimaga station, subauroral glow and auroras were recorded by the full-sky camera Keo Sentry in some emissions [Ievenko, Parnikov, 2022]. Figure 22 presents data from the all-sky cameras at the two stations as keograms on November 4, 2021 at 09:00–11:30 UT. The keogram from the Tixie Bay station (*a*) shows the dynamics of discrete auroras along the meridian in the range of geomagnetic latitudes  $63^{\circ}$ – $71^{\circ}$ . Keograms from the Maimaga station (*b*, *c*) exhibits the dynamics of auroras and subauroral glow in the 557.7 and 630.0 nm [OI] emissions at latitudes  $52^{\circ}$ – $62^{\circ}$ .

The phase of development of a substorm, according to mid-latitude magnetograms, began at ~09:12 UT (see Figure 5) with  $SYM-H \sim -100$  nT. At that time, under conditions of intermittent clouds, a broad brightening of wide radiant auroral band was observed in the 557.7 and 630.0 nm emissions in the vicinity of the zenith of the Maimaga station and a rapid expansion of intense auroras to the pole. The keograms show a short-term increase in the intensity of these emissions with a maximum at  $57^{\circ}$ – $62^{\circ}$  latitudes. An increase in diffuse aurora (DA) was recorded equatorward of discrete auroras (panels *b*, *c*).

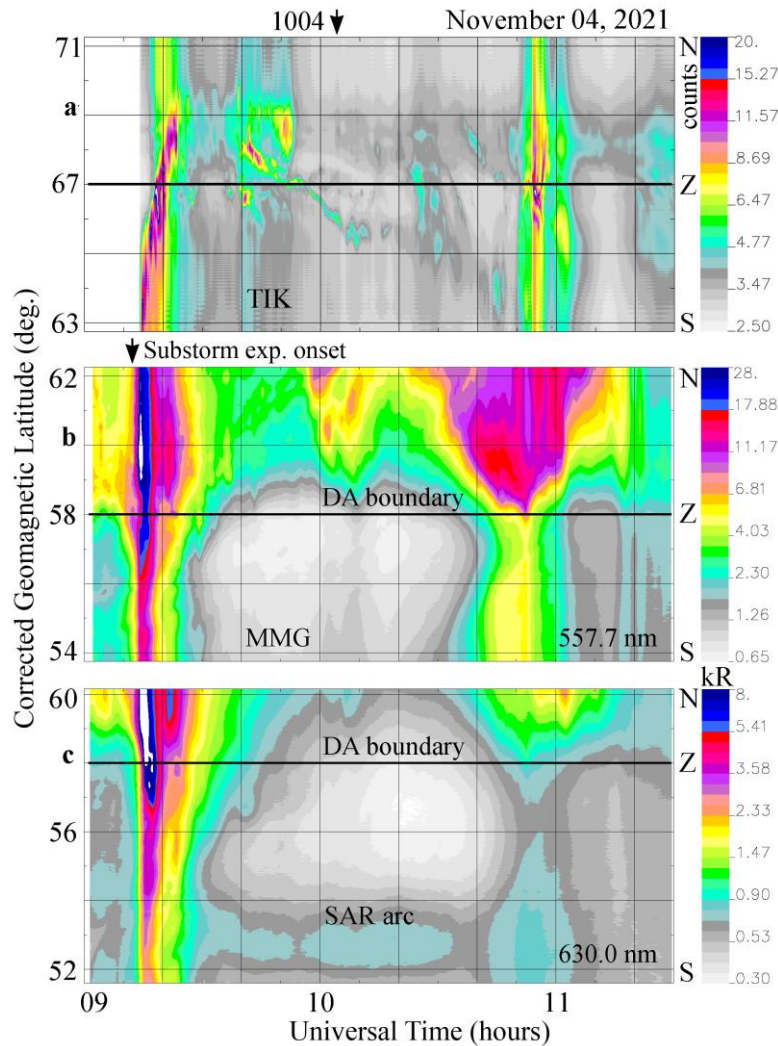


Figure 22. Dynamics of auroras and subauroral glow on the meridian of Yakutsk during the November 3–4, 2021 magnetic storm: *a* — a keogram from the Tixie Bay station projected onto the Earth surface for the 110 km height of auroras in the visible region; *b*, *c* — keograms in the 557.7 and 630.0 nm [OI] emissions from the Maimaga station for the aurora height of 110 and 250 km respectively; Z is the zenith of the observation station. The color emission intensity scales are shown in relative units for the Tixie Bay station and in kR for the Maimaga station

The keogram from the Tixie Bay station (*a*) demonstrates a shift of discrete auroras to the pole from the southern horizon to the geomagnetic latitude of  $\sim 68.5^\circ$  (formation of an auroral bulge).

From  $\sim 09:30$  UT, discrete auroras were observed which moved toward the equator at the Tixie Bay station during the recovery phase of the substorm. At the Maimaga station, after the rapid decay of auroral activity, the DA equatorial boundary was detected in the vicinity of the zenith; and a stable auroral red arc (SAR arc), in the 630.0 nm emission with an intensity 600–900 R on the southern horizon until  $\sim 11:00$  UT.

Figure 23 displays processed images with recording of auroras and subauroral glow across the sky in geomagnetic coordinates. The recording was performed under good atmospheric transparency at 10:04 UT during the recovery phase of the substorm. At that time, intense discrete auroras were observed at the Tixie Bay station (see Figure 23, *a*) at a geomagnetic latitude of  $\sim 66^\circ$  and moved toward the equator as described in the keogram (see Figure 22, *a*, 10:04 UT). The Maimaga station recorded the DA equatorial boundary in the vicinity of the zenith at a latitude of  $\sim 58^\circ$  and discrete auroras on the northern horizon in the two emissions. At 630.0 nm, there was a SAR arc with an intensity of  $\sim 8.00$  R far south of the station with a decrease in geomagnetic latitude to the east.

In Figure 23, *c*, the image is projected onto the Earth surface for a DA height of 250 km in the 630.0 nm emission. For the given height of the red arc 350–400 km, its projection at 10:04 UT was at latitudes  $\sim 50^\circ$ – $53^\circ$  on the meridian of the observation station.

## CONCLUSION

Thus, the comprehensive analysis leads to the following conclusions.

1. The SHICRA SB RAS neutron monitors, installed in Yakutsk and PGO Tixie Bay, recorded the first terrestrial increase in the SCR flux in solar cycle

25. This event was the 73rd since the registration of the first SCR flare on February 28, 1942 and is now known as GLE73, which had a low amplitude to 6 % even at polar CR stations.

2. The M1.7 class solar flare that occurred on November 2, 2021 caused the first powerful Forbush effect in SC 25, which began at the end of November 3. Its amplitude, according to one-minute pressure-corrected NM data from the Tixie Bay station, ran to 18.9 %; from the Yakutsk station, 16.1 %.

3. Using observations from the Yakutsk meridional chain of magnetic stations, we have shown that on November 3, 2021 in the dawn sector north of the Zhigansk station but south of Kotelny Island at a latitude  $61^\circ < \Phi' < 70^\circ$ , a westward electrojet developed in the ionosphere, which deflected by  $\sim 30^\circ$ – $35^\circ$  to the north. The pattern of changes in the magnetic field *H* components at the Zhigansk and Yakutsk stations, located in the dawn sector, fits perfectly into the distribution of magnetic vectors of the global SuperMag network as part of polar current system DP11 and complements the pattern of real magnetic vectors. Data from the AMPERE project on the distributions of magnetic variations at ionospheric heights and field-aligned currents in the dawn sector makes it possible to pinpoint the location of the westward auroral electrojet at  $\Phi' \sim 67^\circ$  N.

4. From measurements of the Yakutsk meridional chain of magnetic stations during the strong geomagnetic storm, we have found that on November 4, 2021 an eastward electrojet took place in the afternoon and dusk sectors at  $56^\circ < \Phi' < 61^\circ$ , and in the late evening and night hours the Zhigansk and Yakutsk stations were under a complex system of ionospheric currents. Data from the AMPERE project on the distributions of magnetic variations at ionospheric heights and field-aligned currents in the dawn sector allows us to specify the location of the eastward auroral electrojet at  $\Phi' \sim 58^\circ$  N.

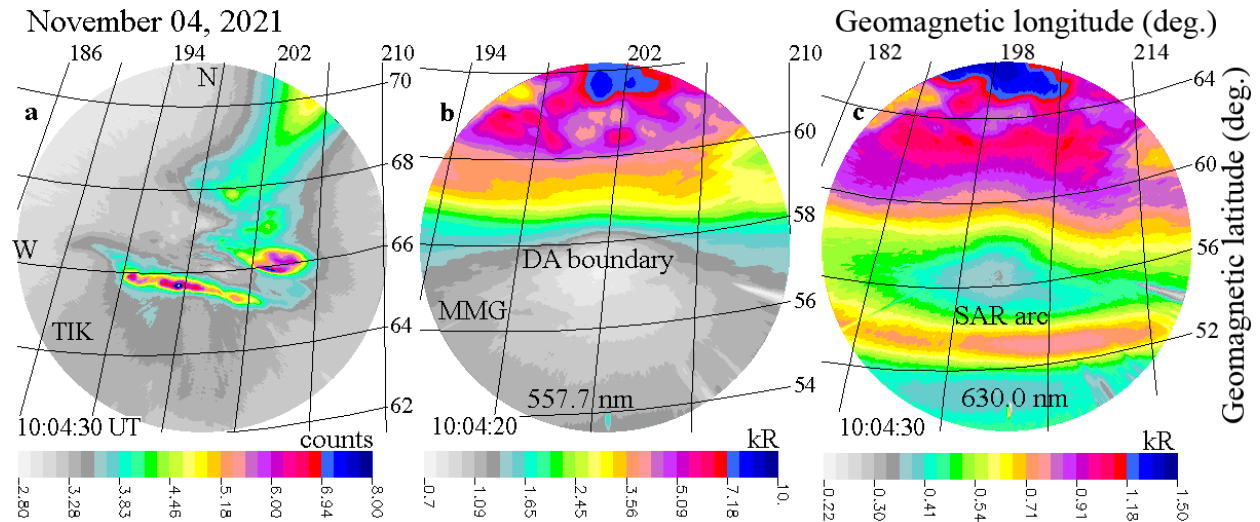


Figure 23. An example of recording of auroras and subauroral glow across the sky at the two stations in the November 4, 2021 event. The processed images projected onto the Earth surface are shown for the 110 km height of discrete auroras at the Tixie Bay station (*a*), for the 110 and 250 km heights of subauroral glow in the 557.7 and 630 nm emissions respectively at the Maimaga station (*b, c*). The emission intensity scales are given in kR (*b, c*); for the Tixie Bay station (*a*), in relative units

5. We have examined interplanetary medium conditions during the development of the strong geomagnetic storm on November 3–11, 2021. Data on variations in SW and *Dst* parameters allows us to assume that the November 3 event defined as an isolated intense substorm is likely to be an element of the initial phase of the described storm.

6. On complete ground freezing, a steeper dependence is observed of the potential difference on the magnetic field strength than with maximum thawing of the top layer of ground. The slope coefficient is eight times higher. The coefficients of dependence observed in early November 2021 are closer in time to the winter ones. The change in these coefficients is associated with a change in ground conductivity.

7. During the events in early November 2021, continuous and quasi-periodic broadband hisses were observed associated with a change in the direction of the IMF  $B_z$  component: a change in the lower and upper frequencies and VLF emission intensity in ranges 1.0–13.5 kHz at 21:00–23:00 UT on November 3, 0.7–4.5 kHz at 01:00–03:00 UT on November 4, 3.0–5.2 kHz at 12:00–13:00 UT on November 4, 2.2–5.0 kHz at 10:10–11:40 UT on November 4. There were also 80–100 s QP hisses at 02:15–02:50 UT on November 4 with a frequency increase in the range 1.6–4.3 kHz.

8. Analysis of amplitude-phase variations recorded during sudden ionospheric disturbances on October 26 – November 2 has shown that VLF signal propagation at a frequency of 11.904 kHz along the meridian in daytime conditions along the 1400 km path can be considered single-mode.

9. We have adopted parameters of the SPA model that is satisfactorily described by a linear function of the logarithm of the product of the X-ray flux and the solar zenith angle cosine averaged along the radio path. We have assessed the change in the effective height of the Earth—ionosphere waveguide from recorded SPAs.

10. Data from the ionospheric station Zhigansk has revealed that during the Forbush effect there was an ionospheric disturbance manifested itself in complete absorption and shielding of HF radio waves. After the active phase of the Forbush effect, the ionospheric station Zhigansk detected a reduction in F2-layer critical frequencies by 1.5–2.0 MHz due to the magnetospheric–ionospheric storm caused by the Forbush effect. Riometric absorption shows that absorption maxima occur during the negative phase of the Forbush effect.

11. No significant variations in the temperature of the neutral atmosphere beyond the noise level were detected during GLE and Forbush decreases.

12. During the initial phase of the development of the substorm, there was a brightening of the wide radiant auroral band in the 557.7 and 630.0 nm emissions in the vicinity of the zenith of the Maimaga station and a rapid expansion of intense auroras to the pole with a maximum at latitudes 57°–62° in the dusk sector of MLT. An increase in DA was recorded equatorward of discrete auroras. A shift of discrete auroras to the pole

from the southern horizon to the geomagnetic latitude of ~68.5° (formation of an auroral bulge) was observed at the Tixie Bay station. During the substorm recovery phase, discrete auroras were seen moving toward the equator. After the rapid decay in auroral activity, the Maimaga station recorded the DA equatorial boundary in the vicinity of the zenith at a latitude of ~58° and a stable auroral red arc (SAR arc) in the 630.0 nm emission with an intensity 600–900 R at geomagnetic latitudes ~50°–53° until ~11:00 UT.

We are grateful to the World Data Center in Kyoto, Japan for geomagnetic index data, to NASA's Goddard Space Flight Center for interplanetary data, to the SuperMag project for geomagnetic data from the global network, to the AMPERE team for data on magnetic vectors and field-aligned currents, and to the AMPERE Scientific Data Center for providing data from the Iridium Communications group due to the support from the National Science Foundation.

The work was financially supported by the Ministry of Science and Higher Education of the Russian Federation for implementation of the State assignment of SHICRA SB RAS.

## REFERENCES

- Baishev D.G., Samsonov S.N., Moiseev A.V., Boroyev R.N., Stepanov A.E., Kozlov V.I., Korsakov A.A., Toropov A.A., Yoshikawa A., Yumoto K. Monitoring and investigating space weather effects with meridional chain of instruments in Yakutia: a brief overview. *Solar-Terr. Phys.* 2017, vol. 3, iss. 2, pp. 25–33. DOI: [10.12737/stp-3220175](https://doi.org/10.12737/stp-3220175).
- Grigoryev V.G., Starodubtsev S.A., Krivoshapkin P.A., Prikhodko A.N., Yegorov A.G. Cosmic ray anisotropy based on Yakutsk station in real time. *Adv. Space Res.* 2008, vol. 41, iss. 6, pp. 943–946. DOI: [10.1016/j.asr.2007.04.072](https://doi.org/10.1016/j.asr.2007.04.072).
- Howard T. *Coronal Mass Ejections: An Introduction, Astrophysics and Space Science Library*. Springer Science+Business Media, LLC. 2011, vol. 376. DOI: [10.1007/978-1-4419-8789-1](https://doi.org/10.1007/978-1-4419-8789-1).
- Ievenko I.B., Parnikov S.G. Relationship of the SAR arc dynamics to substorm injection based on the aurorae observation. Magnetospheric phenomena in the plasmopause vicinity. *Geomagnetism and Aeronomy*. 2022, vol. 62, no. 1-2, pp. 32–49. DOI: [10.1134/S0016793222020098](https://doi.org/10.1134/S0016793222020098).
- Kozlov V.I., Baishev D.G., Pavlov E.A. Variations of Natural Electrical Potentials in the Cryolithozone, Yakutsk. *Izvestiya, Physics of the Solid Earth*. 2022, vol. 58, no. 3, pp. 435–442.
- Krymsky G.F. Diffusional mechanism of the daily variation of cosmic rays. *Geomagnetizm i aeronomiya* [Geomagnetism and Aeronomy]. 1964, vol. 4, pp. 977–986. (In Russian).
- Krymsky G.F., Krivoshapkin P.A., Grigoryev V.G., Skripin G.V., Chuprova V.P. Dynamics of the cosmic ray current behaviour during large-scale solar wind disturbances. *Proc. 28<sup>th</sup> ICRC*. Tsukuba, Japan, 2003, SH 2.2, pp. 3613–3616.
- Kumar A., Kumar S. Solar flare effects on D-region ionosphere using VLF measurements during low- and high-solar activity phases of solar cycle 24. *Earth, Planets and Space*. 2018, vol. 70, no. 29, pp. 1–14. DOI: [10.1186/s40623-018-0794-8](https://doi.org/10.1186/s40623-018-0794-8).
- Kurzhkovskaya N.A., Zotov O.D., Klain B.I. Relationship between geomagnetic storm development and the solar

- wind parameter  $\beta$ . *Solar-Terr. Phys.* 2021, vol. 7, iss. 4, pp. 24–32. DOI: [10.12737/stp-74202104](https://doi.org/10.12737/stp-74202104).
- Loewe C.A., Prolls G.W. Classification and mean behavior of magnetic storms. *J. Geophys. Res.* 1997, vol. 102, no. A7, pp. 14209–14213.
- Manninen J., Kleimenova N.G., Gromova L.I., Fedorenko Y.V., Nikitenko A.S., Lebed' O.M. Daytime VLF emissions during the magnetic storm recovery phase: the event of January 5, 2015. *Geomagnetism and Aeronomy.* 2020, vol. 60, no. 3, pp. 301–310. DOI: [10.1134/S0016793220030111](https://doi.org/10.1134/S0016793220030111).
- Mitra A.P. *Ionospheric Effects of Solar Flares*. Dordrecht, Holland, D. Reidel Publ. Co., 1974, 307 p. (Russ. ed.: Mitra A.P. *Vozdeistvie solnechnykh vspyshek na ionosferu Zemli*. Moscow, Mir Publ., 1977, 370 p.).
- Murzaeva N.N., Mullayarov V.A., Kozlov V.I., Karimov R.R. Morphological characteristics of the midlatitude regular noise background of the natural low-frequency emission. *Geomagnetism and Aeronomy.* 2001, vol. 41, no. 1, pp. 76–83.
- Orlov A.B., Pronin A.E., Uvarov A.N. Latitudinal dependence of the effective electron-loss coefficient in the daytime lower ionosphere as deduced from VLF phase variations and riometric absorption data during SIDs. *Geomagnetism and Aeronomy.* 1998, vol. 38, no. 3, pp. 341–346.
- Rukovodstvo URSI po interpretatsii i obrabotke ionogramm* [URSI Manual on Ionogram Interpretation and Processing]. Moscow, Nauka Publ., 1977, 342 p.
- Starodubtsev S.A., Baishev D.G., Grigoryev V.G., Karimov R.R., Kozlov V.I., Korsakov A.A., Makarov G.A., Moiseev A.V. Analyzing solar, cosmic, and geophysical events in September 2017, SHICRA SB RAS complex observations. *Solar-Terr. Phys.* 2019, vol. 5, iss. 1, pp. 14–27. DOI: [10.12737/stp-51201903](https://doi.org/10.12737/stp-51201903).
- Todoroki Y., Maekawa S., Yamauchi T., Horie T., Hayakawa M. Solar flare induced D region perturbation in the ionosphere, as revealed from a short-distance VLF propagation path. *Geophys. Res. Lett.* 2007, vol. 34, iss. 3, L03103, pp. 1–5. DOI: [10.1029/2006GL028087](https://doi.org/10.1029/2006GL028087).
- Shefov N.N., Semenov A.I., Homich V.Yu. *Izluchenie verhej atmosfery – indikator ee struktury i dinamiki* [Atmospheric Radiation as an Indicator of Its Structure and Dynamics]. Moscow, GEOS Publ., 2006. 741 p. (In Russian).
- Yahnin A.G. Magnetospheric substorm: Main manifestations and possible mechanisms. *Plazmennaya geliogeofizika* [Plasma Heliogeophysics]. Moscow, Fizmatlit Publ., 2008, vol. 1, pp. 465–483. (In Russian).
- Yumoto K., Tanaka Y., Oguti T., Shiokawa K., Yoshimura Y., Isono A., Fraser B.J., Menk F.W., and the 210 degrees MM Magnetic Observation Group. Globally coordinated magnetic observations along 210° magnetic meridian during STEP period, 1, Preliminary results of low-latitude Pc 3's. *J. Geomagnetism and Geoelectricity.* 1992, vol. 44, pp. 261–276.
- URL: <http://www.nmdb.eu> (accessed March 22, 2024).
- URL: <http://stjarnhimlen.se/comp/tutorial.html> (accessed March 22, 2024).
- URL: [https://cdaw.gsfc.nasa.gov/CME\\_list](https://cdaw.gsfc.nasa.gov/CME_list) (accessed April 20, 2023).
- URL: <https://www.spaceweather.com> (accessed April 20, 2023).
- URL: <https://solarmonitor.org> (accessed April 20, 2023).
- URL: <https://planetcalc.ru/7721/?thanks=1> (accessed April 20, 2023).
- URL: <https://spdf.gsfc.nasa.gov/pub/data/omni/> (accessed November 14, 2023).
- URL: [https://wdc.kugi.kyoto-u.ac.jp/ae\\_realtime/](https://wdc.kugi.kyoto-u.ac.jp/ae_realtime/) (accessed April 20, 2023).
- URL: <https://supermag.jhuapl.edu/> (accessed November 14, 2023).
- URL: <https://ampere.jhuapl.edu/> (accessed November 14, 2023)
- URL: [https://wdc.kugi.kyoto-u.ac.jp/dst\\_provisional/index.html](https://wdc.kugi.kyoto-u.ac.jp/dst_provisional/index.html) (accessed November 14, 2023).
- Original Russian version: Kozlov V.I., Starodubtsev S.A., Grigoryev V.G., Baishev D.G., Makarov G.A., Pavlov E.A., Karimov R.R., Korsakov A.A., Stepanov A.E., Koltovskoi I.I., Ammosov P.P., Gavriilyeva G.A., Ievenko I.B., Parnikov S.G., published in *Solnechno-zemnaya fizika*. 2025, vol. 11, no. 1, pp. 10–30. DOI: [10.12737/szf-111202502](https://doi.org/10.12737/szf-111202502). © 2025 INFRA-M Academic Publishing House (Nauchno-Izdatelskii Tsentr INFRA-M)
- How to cite this article*
- Kozlov V.I., Starodubtsev S.A., Grigoryev V.G., Baishev D.G., Makarov G.A., Pavlov E.A., Karimov R.R., Korsakov A.A., Stepanov A.E., Koltovskoi I.I., Ammosov P.P., Gavriilyeva G.A., Ievenko I.B., Parnikov S.G. Analysis of helio- and geophysical events in October–November 2021 from comprehensive observations of SHICRA SB RAS. *Solar-Terrestrial Physics.* 2025, vol. 11, iss. 1, pp. 7–26. DOI: [10.12737/stp-111202502](https://doi.org/10.12737/stp-111202502).